Enhancement Effect of Multi-Stage Inducing Duct on the wind velocity profile

Mojtaba Tahani[a,*], Mehran Masdari[a], Amin Habibi[a], Mojtaba Mirhosseini[b]

[a] Department of aerospace engineering, Faculty of New Sciences and Technologies,

University of Tehran, Tehran, Iran.

[b] School of Advanced Technologies, Iran University of Science and Technology, Tehran, Iran

Abstract

To extracting power from the wind, the high enough velocity of the wind is the key factor. But, winds with high enough velocities are not available in most areas, and therefore, finding a method to enhance the velocity potential of the low-speed winds has been a serious challenge in wind engineering. In this research study, a hollow duct with a specific configuration, we called Multi-Stage Inducing Duct, is presented which is capable to cause a great enhancement in the velocity profile of the low-speed winds, enough to start most of the small horizontal wind turbines. For example, a three-stage inducing duct can increase the wind velocity from 3 m/s to 9.3 m/s on average at the first stage throat of the duct, which equals an increase of 29-times in wind potential power! This configuration of the duct has been introduced, numerically simulated and the effect of its various geometrical parameters investigated. The effects of wind velocity and the number of the stages on the duct performance are investigated, and finally, a study on the relative effectiveness of adding each of the stages is carried out to help us decide where the upper limit for the number of the stages is.

Key words: wind energy, multi-stage inducing duct, inducing suction effect, wind power augmentation, low-speed winds.

1. Introduction

For years, fossil fuels were the main source of energy in the world. But, global warming and the environmental pollutions caused by fossil fuels forced scientists to think of finding some clean alternative energy sources. Wind as a green source of energy has received a lot of attention in recent years and most of the countries are planning to develop wind power plants. Wind turbines are machines that extract mechanical power from the wind and mainly there are two types of wind turbines: the vertical axis wind turbines (VAWTs), and the horizontal axis wind turbines (HAWTs). Tahani et al. (2016) studied a straight blade vertical axis wind turbine using double multiple stream tube (DMST) theory. First, a DMST code was developed and validated with existing experimental results, and then the VAWT design was optimized using a novel heuristic method they presented [1]. Tahani et al. (2017) designed and numerically investigated a Savonius vertical axis wind turbine with discharge flow directing capability. They modified the design of the turbine and showed that using a twisted Savonius wind turbine with a conical shaft improves the power coefficient by 18% compared to a simple Savonius wind turbine [2]. Tahani et al. (2017) investigated the effect of geometrical parameters on the performance of a horizontal axis wind turbine in different turbulence intensities using the blade element momentum theory (BEM). After the results of the BEM algorithm were validated using existing experimental data, the shape of the blades was optimized using the popular ant colony optimization algorithm. They showed optimizing the geometry

causes delation in the flow separation and therefore, more power can be extracted [3]. Tahani et al. (2017) aerodynamically designed and optimized a 1 mega-Watt horizontal axis wind turbine based on the blade element momentum theory (BEM). Using a new linearization method, they considered linear distributions for chord lengths and twist angles of the blade cross-sections, and the optimum linearized distributions were obtained considering the power coefficient as the optimization criterion [4]. Finding a solution to extract power from the wind, despite its stochastic nature, helps us to use this source of energy in many situations that the wind does not blow at high enough velocity and enough hours of the day. Using hybrid methods is a way to extract power from the wind even though the wind does not blow at enough hours of the day. In 2015, Tahani et al. optimized a hybrid system for a three-story building in Tehran, the capital of Iran [5]. In the case of low velocity of the wind, using a duct is an old solution to increase the wind velocity enough to an economic power generating. Duct augmentation to enhance the power generated by a wind turbine has been the subject of various researches. Abe et al. (2005) carried out both experimental and numerical investigation of the flow field of a small wind turbine with a flanged diffuser [6]. Ohya et al. (2008) experimentally investigated the effects of various geometrical characteristics of a flanged diffuser on the performance of a flange-ducted wind turbine. They reported a power augmentation of 4-5 compared to the bare turbine [7]. Kosasih et al. (2012) experimentally investigated a micro ducted wind turbine. They studied the effects of the shape and geometrical features of the shroud [8]. Jafari et al. (2014) numerically simulated a small wind turbine equipped with a simple frustum diffuser [9]. Mansour et al. (2014) investigated flow fields around flanged diffusers using computational fluid dynamics [10]. In recent years, some researchers developed new ideas to extract power from low-speed winds. Zabihzadeh et al. (2015) suggested putting a step inside the diffuser to cause the separation and achieve more suction due to the low-pressure region caused by the separation. [11]. Han et al. (2015) introduced a new duct that was able to increase the wind velocity effectively and extract power from the low-speed winds [12]. Al-Sulaiman (2017) brought up the idea of putting an ejector at the outlet of the wind turbine duct to increase the duct suction [13]. Khamlaj et al. (2018) computationally investigated a flanged diffuser-augmented wind turbine using open source code software OpenFOAM [14]. Saleem et al. (2019) investigated the effect of rotor tip clearance on the aerodynamic performance of an airfoil-based ducted wind turbine [15]. Noorollahi et al. (2020) carried out a numerical investigation of the flow around a small ducted wind turbine [16]. Keramat et al. (2020) presented the idea of using a variable and controllable nozzle-diffuser duct with a wind turbine [17]. Bontempo et al. (2020) conducted a review and assessment of the most important theoretical models conceived for the performance analysis and design of the diffuser augmented wind turbines [18]. Keramat et al. (2020) presented a mathematical model of a shrouded wind turbine and showed using a properly designed duct, the power coefficient of 0.93 can be reached [19]. Prasad et al. (2020) computationally studied three types of diffuser ducts: straight ducts, curved ducts, and Vortex Generators (VGs) ducts. They also studied the effect of brimmed ducts and reported an improvement in power particularly about curved ducts and VGs ducts [20]. Rivarolo et al. (2020) investigated the effect of yaw angle on the performance of a convergent-divergent ducted wind turbine [21]. Avallone et al. (2020) studied the effect of the tip-clearance ratio on the aeroacoustics of a diffuser-augmented wind turbine [22]. Nardecchia et al. (2021) analyzed a mini ducted wind turbine utilizing numerical simulation. They compared the results with those of a similar turbine installed in the open field and reported an increase of up to 432% in the extracted energy thanks to the use of the duct [23].

In this research study, a specific duct configuration for horizontal wind turbines is introduced that can provide a great augmentation in wind velocity profile compared to other presented ducts. This configuration, called "Multi-Stage Inducing Duct", is shown in fig. 1 and fig. 2. In this configuration, each downstream stage strengthens the suction produced by its upstream stage, and finally, the maximum suction occurs at the first stage throat, where the wind turbine should be placed there.

All stages are supposed to be cast of aluminum, due to its lightness, acceptable strength, as well as its stainless properties. A value of 4 mm is designated to the body thickness of all the stages. At the two ends

of all stages (at the inlet of nozzles and the outlet of diffusers), edges are designed rounded (circular) as shown in fig. 3. To emphasize the thickness of the stage body, fig. 3 is illustrated exaggerated.

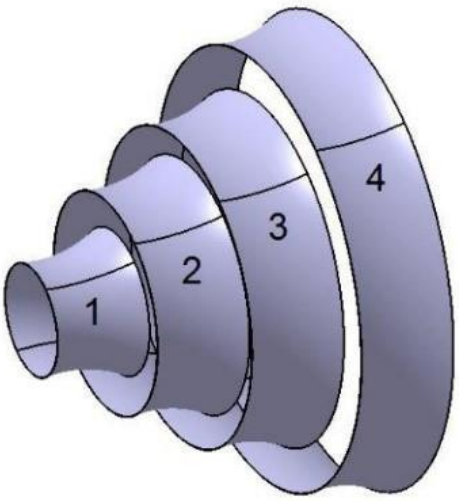

Fig. 1. Configuration of the multi-stage inducing duct

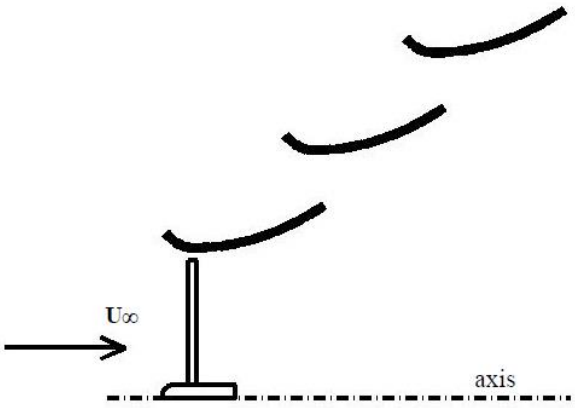

Fig. 2. Schematic lateral view of the multi-stage inducing duct

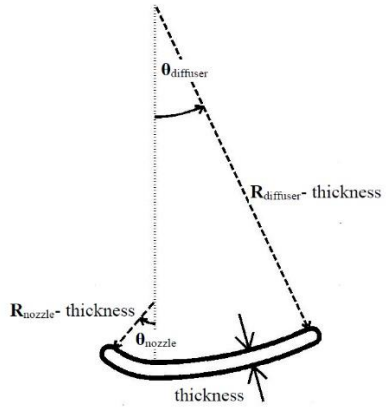

Fig. 3. An exaggerated schematic of a stage to emphasize the thickness.

2. Numerical method

2.1. Governing equations

The general form of the continuity and momentum conservation equations are as follows:

$$\frac{\partial \rho}{\partial t} + \frac{\partial}{\partial x_i}(\rho u_i) = 0 \qquad (1)$$

$$\frac{\partial}{\partial t}(\rho u_i) + \frac{\partial}{\partial x_j}(\rho u_i u_j) = -\frac{\partial P}{\partial x_i} + \frac{\partial \tau_{ij}}{\partial x_j} + \rho g_i + F_i \qquad (2)$$

Where ρ is the fluid density, x_i and u_i are the length and velocity components in i^{th} spatial direction, respectively. P is the static pressure, g_i and F_i represent the gravitational acceleration and body forces in i^{th} spatial direction, respectively. The time derivatives are zero for our steady flow. Also, the density is constant since we study a low-speed flow. The term τ_{ij} is the Reynolds stress tensor that is defined as:

$$\tau_{ij} = \mu\left(\frac{\partial u_i}{\partial x_j} + \frac{\partial u_j}{\partial x_i}\right) - \frac{2}{3}\mu\left(\frac{\partial u_i}{\partial x_i}\right)\delta_{ij} \qquad (3)$$

Where δ_{ij} is the Kronecker delta, which equals 1 when i and j are the same, and equals 0 otherwise. From the equations (1)-(3), in the absence of the body forces, and neglecting the effects of the gravity, the Reynolds averaged momentum equation can be derived as:

$$\frac{\partial}{\partial t}(\rho u_i) + \frac{\partial}{\partial x_j}(\rho u_i u_j) = -\frac{\partial P}{\partial x_i} + \frac{\partial}{\partial x_j}\left[\mu\left(\frac{\partial u_i}{\partial x_j} + \frac{\partial u_j}{\partial x_i}\right) - \frac{2}{3}\mu\left(\frac{\partial u_i}{\partial x_i}\right)\right] + \frac{\partial\left(\overline{u_i' u_j'}\right)}{\partial x_j} \qquad (4)$$

The term $\overline{u_i' u_j'}$ which is related to the turbulence appears in the momentum equation and should be expressed using a suitable turbulence model [20].

2.2. Turbulence model

In this study, the k-ω based Shear Stress Transport (SST) turbulence model with automatic wall functions (mixed formulation) developed by Menter is used. K represents the turbulence kinetic energy, and ω is the turbulence specific dissipation rate. The SST k-ω turbulence model uses a combination of k-ω and k-ε turbulence models using a blending function that is able to change the model from k-ω to k-ε when the distance from the wall increases. Thus, the SST k-ω turbulence model benefits the high convergence rate

of the k-ε high-Reynolds model away from the surface, beside the high accuracy of the k-ω model near the wall [20]. This two-equation model is the most appropriate RANS-based turbulence model for predicting flow separation [24]. Generally, the SST k-ω turbulence model can be formulated as follows [20] , [24]:

$$\frac{\partial(\rho k)}{\partial t}+\frac{\partial(\rho u_j k)}{\partial x_j}=P-\beta^*\rho\omega k+\frac{\partial}{\partial x_j}\left[(\mu+\sigma_k\eta_t)\frac{\partial k}{\partial x_j}\right] \quad (5)$$

$$\frac{\partial(\rho\omega)}{\partial t}+\frac{\partial(\rho u_j\omega)}{\partial x_j}=\frac{\lambda}{v_t}P-\beta^*\rho\omega^2+\frac{\partial}{\partial x_j}\left[(\mu+\sigma_\omega\eta_t)\frac{\partial\omega}{\partial x_j}\right]+2(1-F_1)\frac{\rho\sigma_{\omega2}}{\omega}\frac{\partial k}{\partial x_j}\frac{\partial\omega}{\partial x_j} \quad (6)$$

$$P=\min\left\{\tau_{ij}\frac{\partial u_i}{\partial x_j},20\beta^*\rho\omega k\right\} \quad (7)$$

$$\tau_{ij}=\eta_t\left(\frac{\partial u_i}{\partial x_j}+\frac{\partial u_i}{\partial x_i}-\frac{2}{3}\frac{\partial u_k}{\partial x_k}\delta_{ij}\right)-\frac{2}{3}\rho k\delta_{ij} \quad (8)$$

Where the turbulent eddy viscosity is:

$$\eta_t=\frac{\rho a_1 k}{\max(a_1\omega\ ,\omega F_2)} \quad (9)$$

The blending functions F_1 and F_2 are as follows:

$$F_1=\tanh\left\{\left\{min\left[max\left(\frac{\sqrt{k}}{\beta^*\omega y}\ ,\frac{500\nu}{y^2\omega}\right),\frac{4\rho\sigma_{\omega2}k}{CD_{k_\omega}y^2}\right]\right\}^4\right\} \quad (10)$$

$$F_2=\tanh\left\{\left[max\left(\frac{2\sqrt{k}}{\beta^*\omega y}\ ,\frac{500\nu}{y^2\omega}\right)\right]^2\right\} \quad (11)$$

Where y is the distance to the nearest wall, and CD_{k_ω} is:

$$CD_{k_\omega}=max\left(2\rho\sigma_{\omega2}\frac{1}{\omega}\frac{\partial k}{\partial x_i}\frac{\partial\omega}{\partial x_i},10^{-10}\right) \quad (12)$$

Far enough from the wall, F_1 equals 0 and the model switches to the k-ε model. Whereas, near the wall (inside the boundary layer), F_1 equals 1 and the model switches to the k-ω model. More details on the above equations can be found in ref [24].

2.3. Details of the utilized numerical algorithm

The flow field around the hollow duct is simulated as an axisymmetric flow using ANSYS-FLUENT commercial software. To pressure-velocity coupling, a coupled solver is applied to solve the system of coupled equations in a steady pressure-based algorithm. The SST k-ω turbulence model described in the previous subsection is used to model the flow turbulency. For spatial discretization, the least-squares cell-based method is used to compute the gradients, and a second-order accuracy is chosen to pressure interpolating. The high accurate power-law scheme is utilized to calculate all the fluxes. The values of the residuals of continuity, momentum, turbulence kinetic energy, and specific turbulence dissipation rate were monitored to decide on the convergence of the numerical method. Calculations stopped when all residuals were less than 10^{-6}. Selecting the double-precision option beside mentioned high accuracy schemes has provided an accurate numerical simulation that is in good agreement with the experimental results (section 3). The computational domain containing 6 zones with the specified boundary conditions is shown in fig. 4.

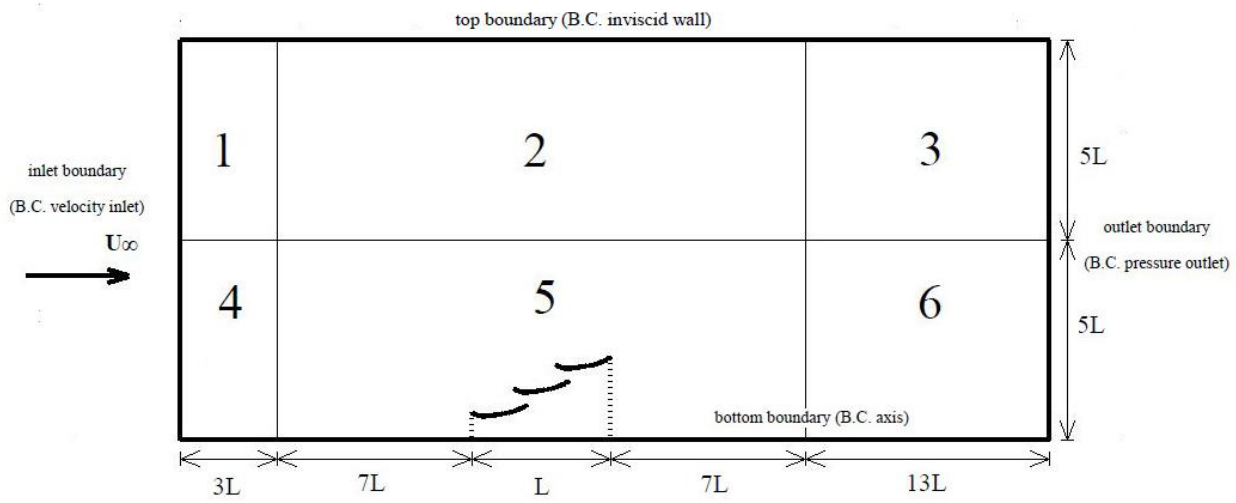

Fig. 4. Computational domain and boundary conditions

2.4. Grid generation

As shown in fig. 4, the computational domain has been divided up to 6 rectangular zones. A triangle non-structured mesh is used for the part contains the bodies (zone 5) due to high ability of triangle non-structured mesh in capturing the geometrical complexities of the model (fig. 5). At other parts of the domain (zones 1,2,3,4,6), that are far enough away from the bodies, a simple uniform orthogonal structured mesh is used due to its simplicity and high convergence rate. To satisfy the requirements of the SST K-Ω turbulence model for acceptable range of the wall y^+, a suitable amount of first layer thickness at boundary layer has been modified from the former numerical experiences and some trial and errors until the acceptable ranges of the wall y^+ be achieved. Diagrams of the average and maximum values of y^+ at all walls (all stages bodies) are illustrated in fig. 6. As can be seen in the diagrams, y^+ is in an acceptable range that confirms the correctness of the chosen first layer thickness.

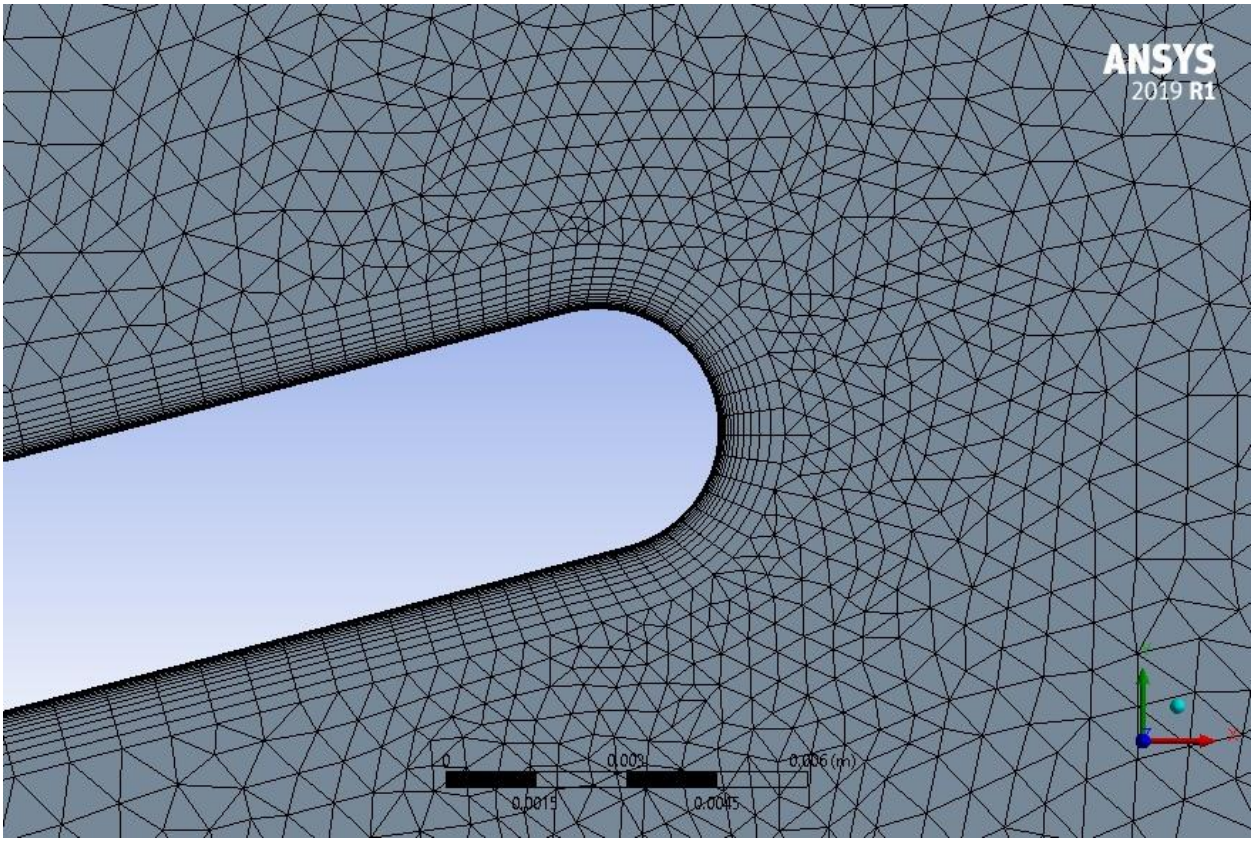

Fig. 5. Mesh that be used in the part of the domain that contains the stages (zone 5 in fig. 4)

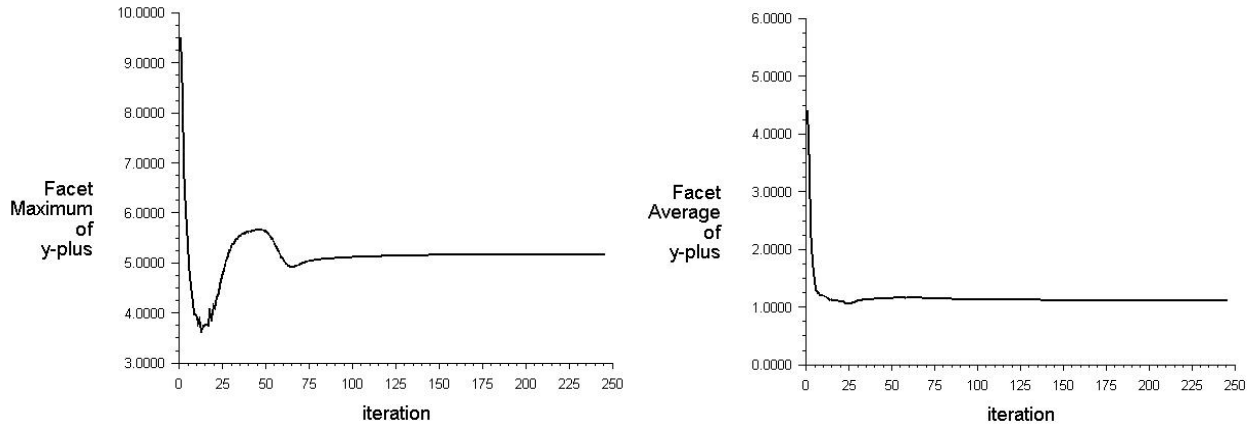

(a) (b)

Fig. 6. Diagram of the maximum wall y^+ at all stages bodies (a), and diagram of the average wall y^+ at all stages bodies(b).

Grids with various sizes are tested to find the suitable size of the grid. The mesh independency diagram is shown in fig. 7. As can be seen in the diagram, a grid with about 82000 cells is enough, and then the results are independent of the size of the grid.

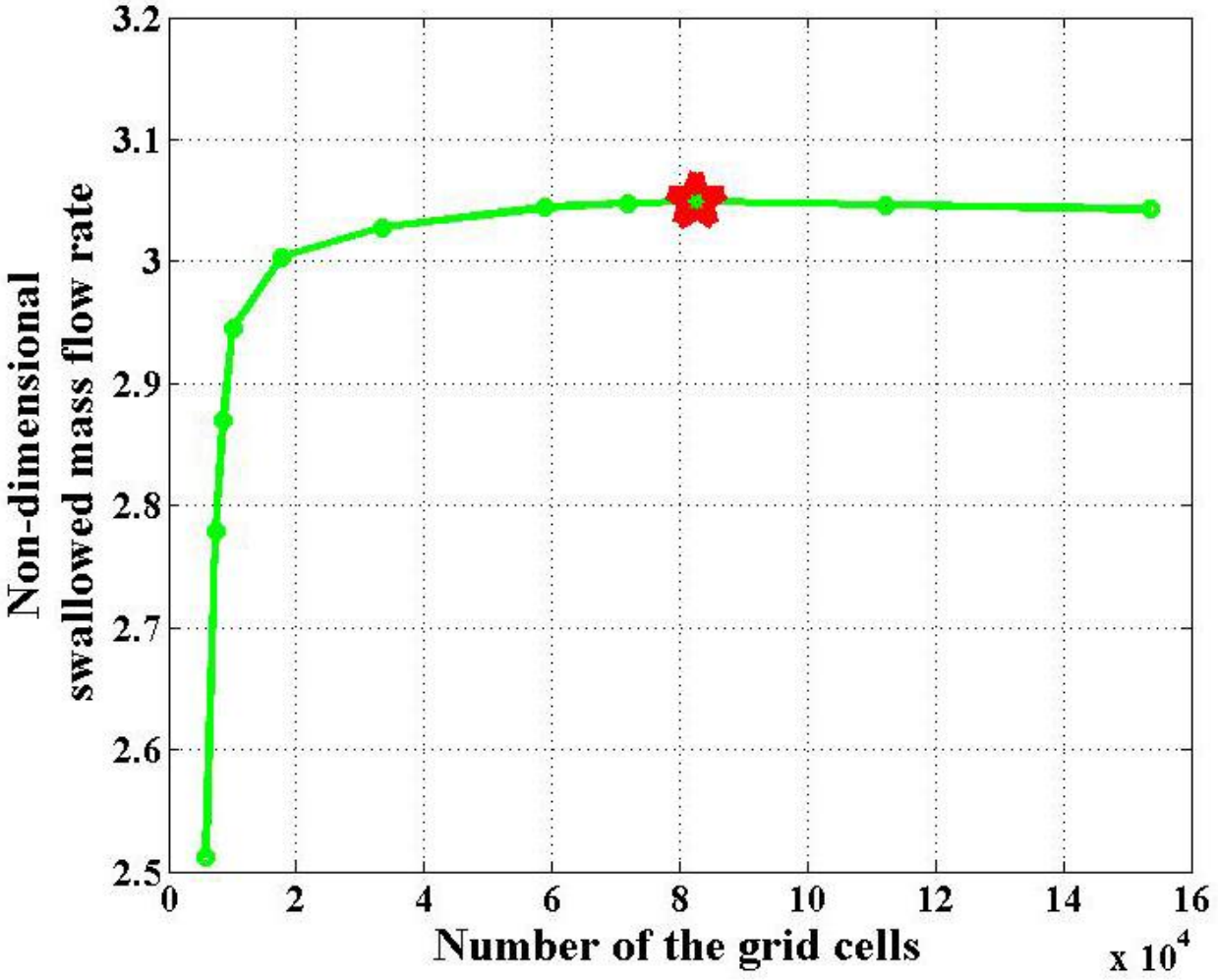

Fig. 7. Grid independency diagram. Suitable size of the grid marked by star on the diagram. Non-dimensional swallowed mass flow rate is defined by eq. 5.

3. Validation of the CFD simulation

3.1. General description

Published experimental results of a hollow flanged duct tested in a wind tunnel at the velocity of 5 m/s performed by Ohya et al. [13] are used to validate the numerical method applied in this study. Flow field around our case and the case they studied both contain a region of negative pressure at the inlet of the duct, then a region of adverse pressure gradient inside the diffuser, and finally, a large region of separation at the end of the duct.

3.2. Wind tunnel experiment

Ohya et al. [13] used the large boundary layer wind tunnel of the Research Institute for Applied Mechanics, Kyushu University to test various hollow-structure ducts. The wind tunnel had a 3.6m wide * 2m high * 15m long measurement section and the maximum wind velocity was 30 m/s. The models were hung in the center of the wind tunnel section, supported by strings. An I-type hot-wire and a static pressure tube using a traversing system were used to measure the distribution of the axial velocity u and the static pressure P along the axis line of the models. The model entrance diameter D=0.2 m was the representative scale length of the model, the wind velocity was $U\infty$=5 m/s, and the Reynolds number was Re=6.8 * 10^4 [13].

3.3. comparing the numerical and experimental results

A schematic view of the duct tested in the wind tunnel is shown in fig. 8. In order to validate the numerical method used in this study, we modeled a hollow duct with a large flange (h/D=0.625), and all of the other parameters are chosen exactly the same as what was given in ref. [13]. The axial velocity along the central axis line of the duct, measured in the wind tunnel, is used to validate the numerical method applied in this study. Fig. 9 shows the numerical results compared to the experimental results published in ref. [13]. As can be seen in the figure, there is a very good agreement between the numerical and experimental results.

4. Results and discussion

4.1. Introducing the parameters reported as results

In this part, some parameters that will be used frequently in the result diagrams are introduced. The amount of the mass flow rate swallowed by a multi-stage duct is the main parameter to evaluate the performance of the duct. The profile of the axial velocity distribution versus the radial distance from the axis, at the throat of the first stage of a multi-stage duct, like what shown in fig. 10, is used to compute the non-dimensional mass flow rate swallowed by the duct at the first stage throat as follows:

$$\mathrm{NDSMFR} = \frac{\int_{r=0}^{r=R_{throat}} \rho v_{axial(r)} 2\pi r dr}{\rho\left(\pi R_{throat}^2\right) U_\infty} \qquad (13)$$

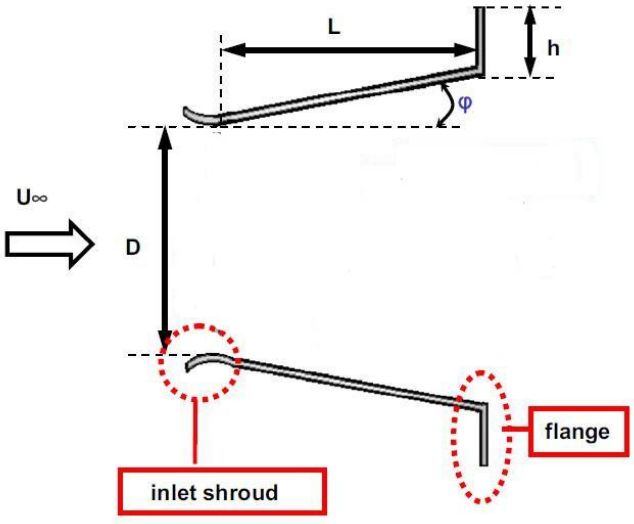

Fig. 8. Schematic of the flanged duct tested in the wind tunnel in ref. [13]

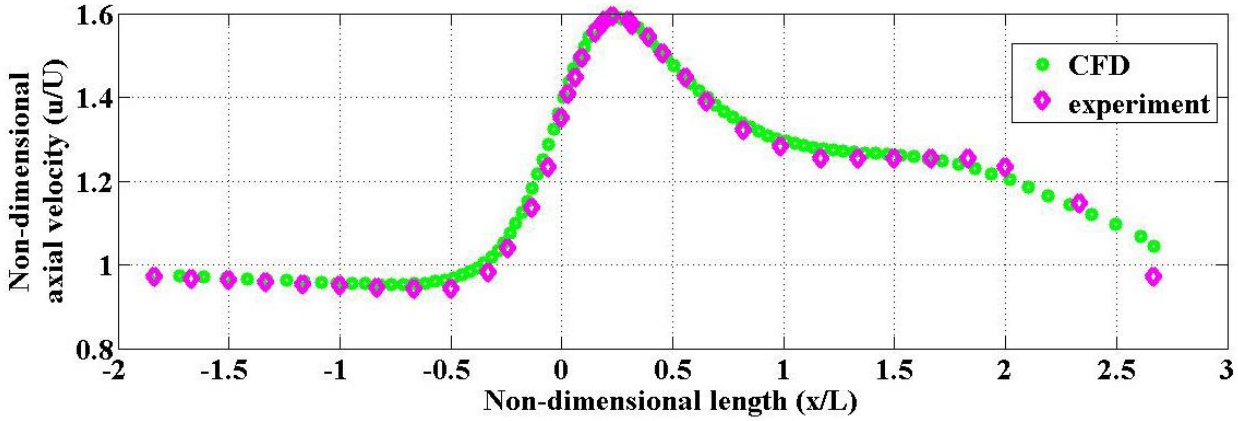

Fig. 9. Validating diagram; x represents the axial distance from the throat in the direction of the flow, and L as shown in fig.8, is the axial distance between the throat and the flange. u is the axial velocity at the position x on the central axis line of the duct and U is the wind tunnel velocity and equals 5m/s. (experimental results from ref. [13]).

Where NDSMFR stands for non-dimensional swallowed mass flow rate, and R_{throat} is the radius of the first stage throat cross-section of the multi-stage duct. Also, r is the radial distance from the duct axis in the first stage throat cross-section plane, $v_{axial(r)}$ is the axial velocity as a function of r, and U_{∞} is the free stream velocity.

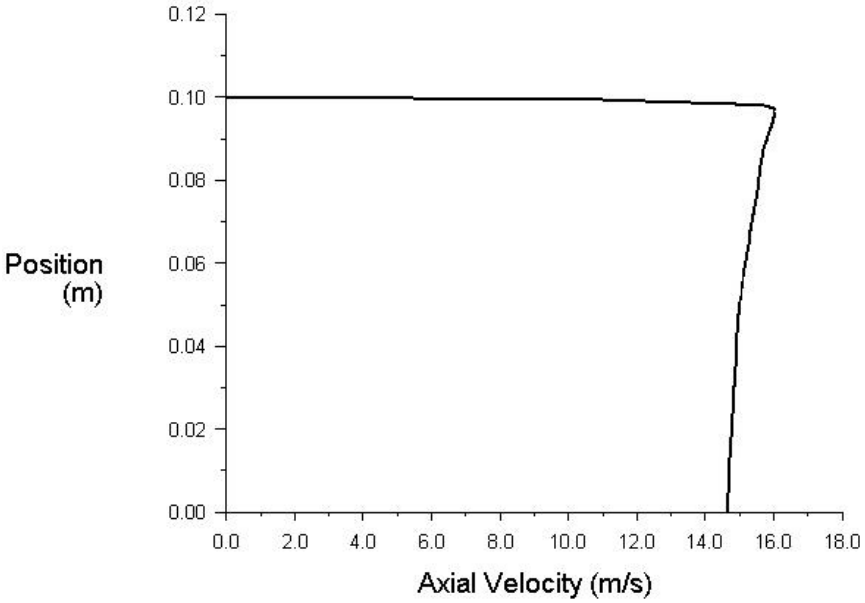

Fig. 10. Profile of the axial velocity versus the radial position from the axis at the first stage throat of a three-stage inducing duct at the wind velocity of 5 m/s.

Also, we can compute the average velocity at the throat of the first stage of a multi-stage duct as follows:

$$v_{average} = \frac{1}{A_t}\int_{r=0}^{r=R_{throat}} v_{axial(r)}\, 2\pi r dr \qquad (14)$$

Where A_t is the area of the cross-section of the first stage throat. Since we are discussing a hollow duct and there does not exist a turbine inside, we can't speak about the generated power. Instead, we introduce a new quantity called "swallowed power" to provide a criterion to evaluate the magnitude of the power

augmentation caused by the duct. The swallowed power is the amount of the flow kinetic energy swallowed by the throat cross-section of the first stage of the duct computed as follows:

$$swallowed\ power = \int_{r=0}^{r=R_{throat}} [\frac{1}{2}\rho v_{axial(r)}^{3}]2\pi r dr \qquad (15)$$

To have a criterion to evaluate the computed values of power, the concept of "a duct with zero stages" is important, and the power swallowed by the first stage throat cross-section of such an imaginary duct has been chosen as the "reference power" as follows:

$$reference\ power = \frac{1}{2}\rho(\pi R_{throat}^{2})U_{\infty}^{3} \qquad (16)$$

The chosen reference power is the power swallowed by the same surface as the first stage throat of a multi-stage duct if there is not any duct, and the mentioned surface is exposed to the free stream. To the swallowed power be independent of the geometrical sizes, the non-dimensional swallowed power (NDSP) is defined as follows:

$$\text{NDSP} = \frac{swallowed\ power}{reference\ power} \qquad (17)$$

The values of the swallowed power and reference power are computed from eq. (15) and eq. (16), respectively.

4.2. Single-stage duct analysis

4.2.1. General description

Since a multi-stage inducing duct consists of some converging-diverging ducts, called stages, studying the performance of a single converging-diverging duct is important. In this section, a single stage is studied and effect of its geometrical parameters is investigated. Fig.11 shows the contours of pressure, velocity and streamlines of the flow field around a single-stage duct. Details of the simulation are given in tabs. 1, 2 and 3.

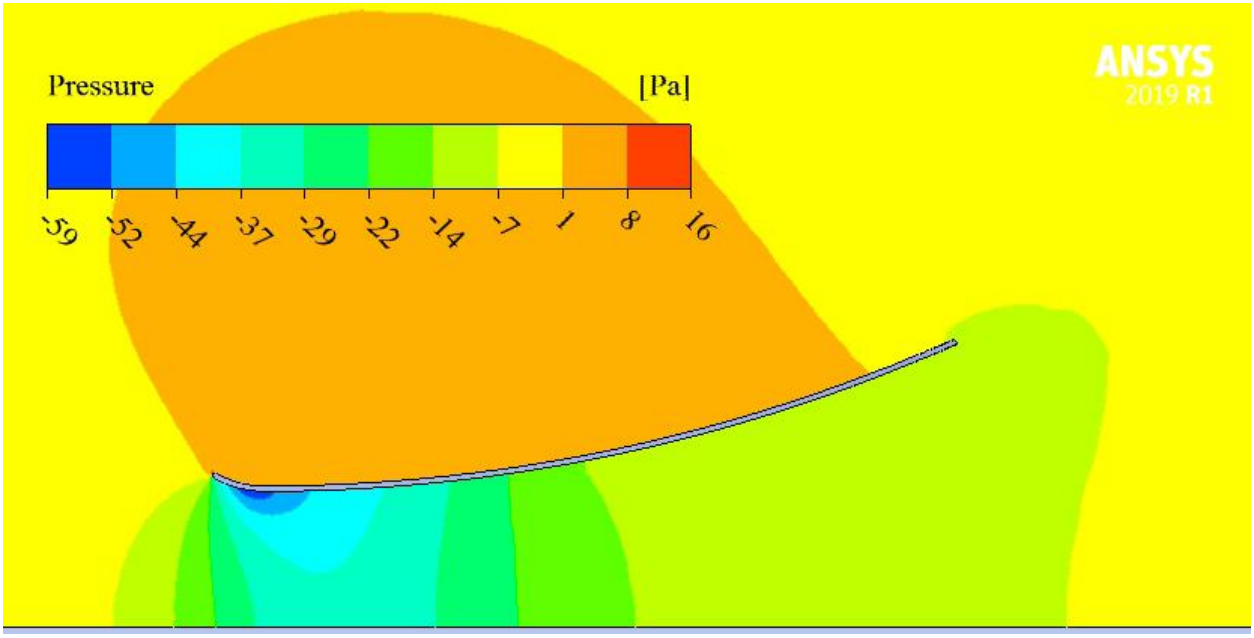

(a)

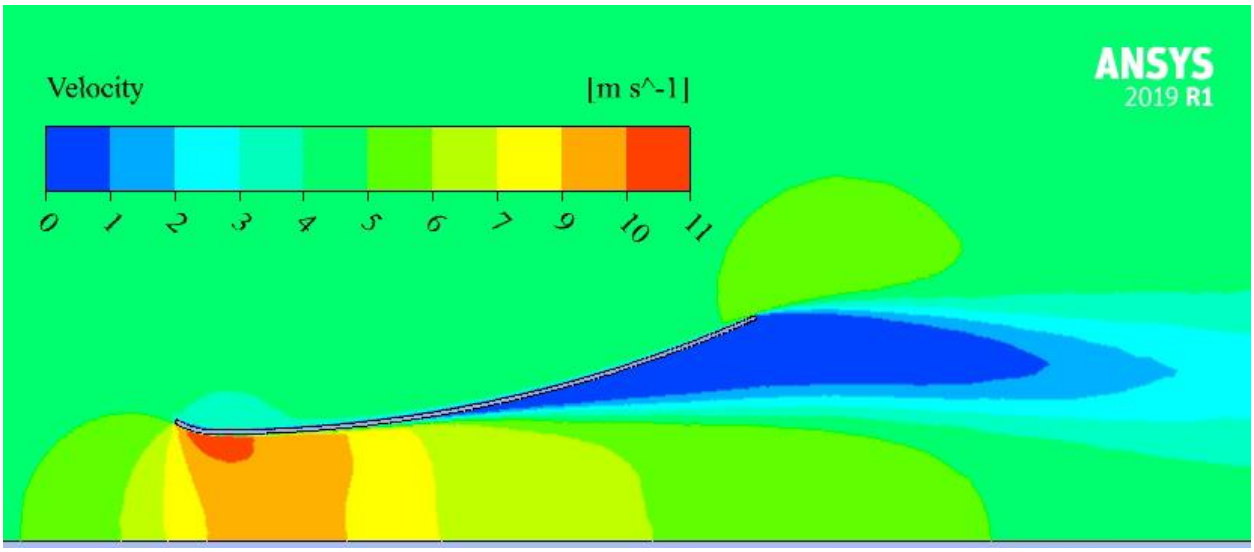

(b)

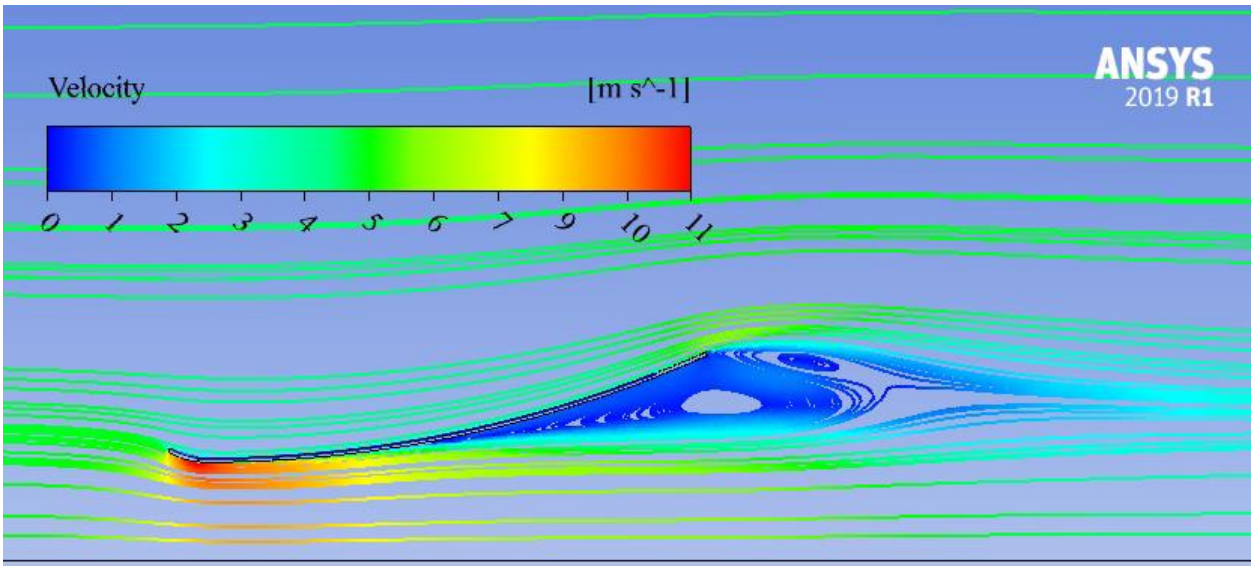

(c)

Fig.11. flow field around a single-stage duct: contour of pressure distribution (a); contour of velocity distribution (b); streamlines(c).

Schematic of a single-stage duct is shown in fig. 12. As can be seen in the figure, the longitudinal-sections of the duct act like a system of airfoils their lift forces neutralize each other due to the axisymmetric geometry of the duct. But their generated circulations boost each other and generate a low-pressure region at the inlet of the duct. As can be seen in the contours, a low-pressure region is generated at the inlet of the duct and swallows the flow inside the duct.

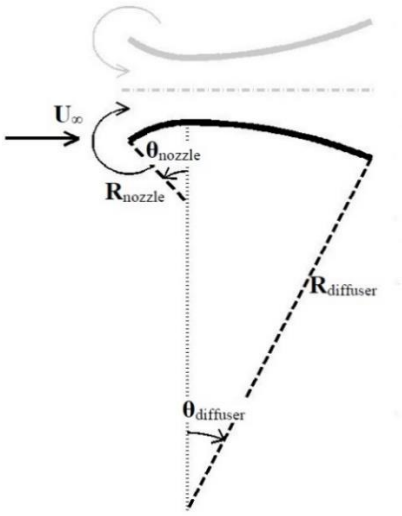

Fig. 12. Schematic of a single-stage duct

4.2.2. Test plan (for single-stage tests)

A single-stage duct with geometric parameters that expressed in tab. 1, has been chosen as the reference geometry. When the effect of each parameter is studied, all other parameters are fixed and equal the reference case (tab. 1). The reference case geometry should be as general as possible so that the effect of all parameters can be seen without being affected by unsuitable values specified to other parameters. For example, we won't be able to observe the effect of the $\theta_{diffuser}$ properly, if the value specified to $R_{diffuser}$ is too small.

Parameter	Value
R_{throat}	0.1 m
non-dimensional R_{nozzle} (R_{nozzle} /R_{throat})	0.75
θ_{nozzle}	30°
non-dimensional $R_{diffuser}$ ($R_{diffuser}$ /R_{throat})	12.5
$\theta_{diffuser}$	24°

Table 1. geometrical parameters of the reference case chosen for all single-stage numerical tests.

Properties of the air and the free stream at which all numerical simulations (including single-stage, dual-stage, and multi-stage cases) performed expressed in tab. 2 and tab. 3, respectively.

Parameter	Temperature (° C)	Density (kg/m^3)	Viscosity (kg/m.s)
Value	15	1.225	$1.7894*10^{-5}$

Table 2. air properties

Parameter	Axial velocity (m/s)	Radial velocity (m/s)	Turbulence intensity (%)	Turbulence viscosity ratio (%)
Value	5	0	5	10

Table 3. free stream properties

4.2.3. Effect of nozzle angle (θ_{nozzle})

Effect of nozzle angle is studied in this part and the results are shown in fig. 13. All other geometric parameters are fixed as in tab.1 and only the nozzle angle varies.

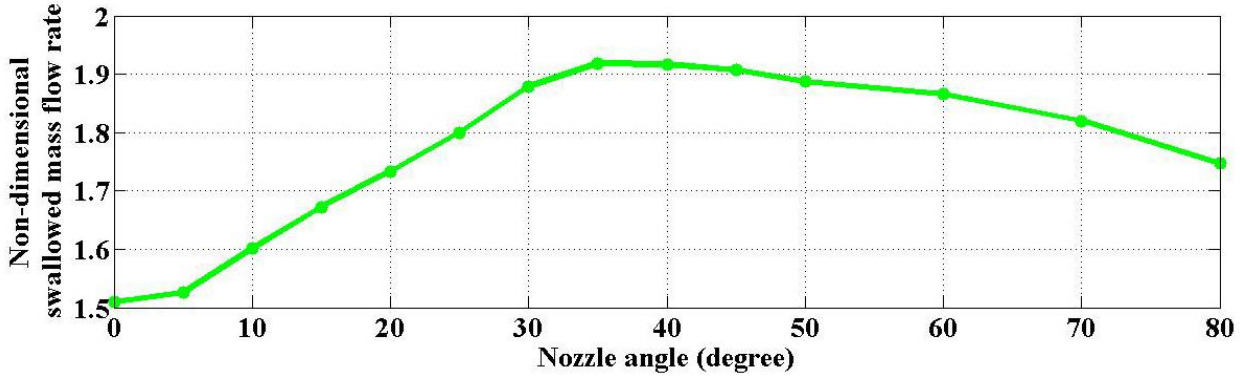

(a)

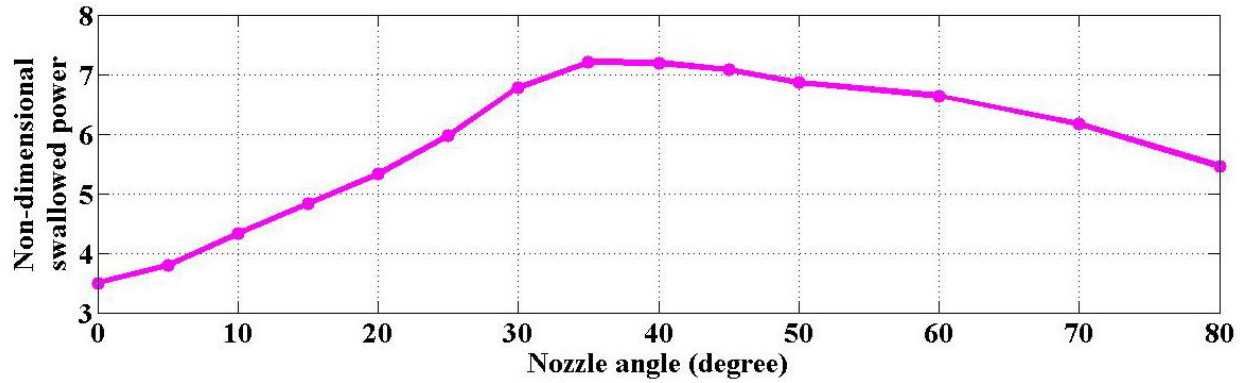

(b)

Fig. 13. Effect of nozzle angle (θ_{nozzle}). (a) Non-dimensional swallowed mass flow rate vs θ_{nozzle} and (b) Non-dimensional swallowed power vs θ_{nozzle}

If we imagine the longitudinal section of the duct as an airfoil (fig. 12), when the nozzle angle increases, the camber of this airfoil will be increased that causes more circulation resulting in more suction and finally more mass flow rate swallowed by the duct. But as the angle of the nozzle rises, the blockage effect due to larger cross-section of the nozzle rises as well, that tries to decrease the mass flow rate swallowed by the duct. When the nozzle angle is small, the blockage effect is small as well and the mentioned effect of the increase in the camber is the dominant factor and the swallowed flow increases as the nozzle angle increases. But when the nozzle angle increases too much, the blockage effect rises and becomes the dominant factor and as can be seen in the diagram, further increase in the nozzle angle causes the swallowed flow starts decreasing.

4.2.4. Effect of nozzle radius (R_{nozzle})

Effect of nozzle radius is studied in this part and the results are shown in fig. 14. All other geometric parameters are fixed as in tab.1 and only the nozzle radius varies.

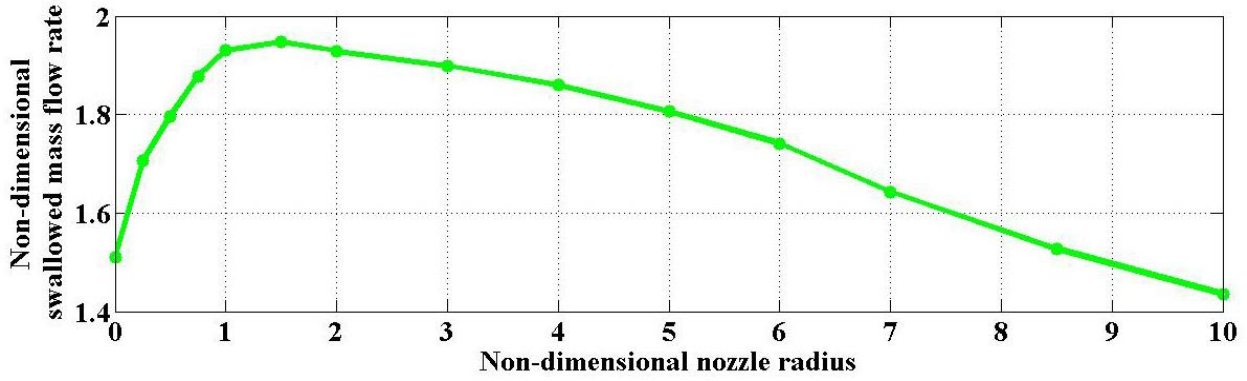

(a)

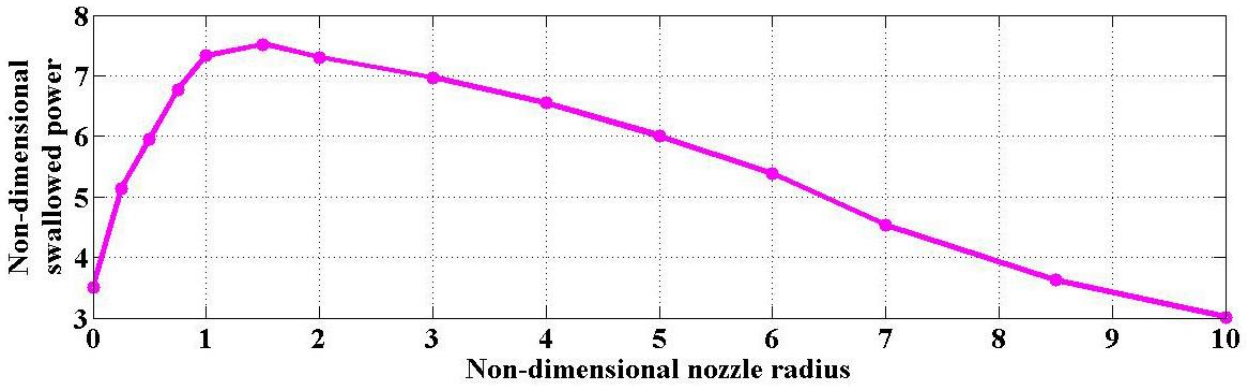

(b)

Fig. 14. Effect of non-dimensional nozzle radius (R_{nozzle}/R_{throat}). (a) Non-dimensional swallowed mass flow rate and (b) Non-dimensional swallowed power.

Similar to previous section, if we imagine the longitudinal profile of the duct as an airfoil (fig. 12), when the nozzle radius is small, increase in the nozzle radius results in increase in the camber of the airfoil, that causes increase in the circulation and suction and finally increase in the mass flow rate swallowed by the duct. But as the radius of the nozzle rises, the blockage effect due to the larger cross-section of the nozzle rises as well that tries to decrease the swallowed flow by the duct. At first the nozzle radius and the blockage effect cause by it are small and the mentioned increasing effect due to increase in the nozzle radius is the dominant factor and the swallowed flow increases. But with further increase in the nozzle radius, the blockage effect rises and becomes the dominant factor and the swallowed flow starts decreasing as the nozzle radius increases.

4.2.5. Effect of diffuser angle ($\theta_{diffuser}$)

In this section, effect of the diffuser angle ($\theta_{diffuser}$) is studied and the results are shown in fig. 15. All other geometrical parameters are fixed as in tab.1 and only the diffuser angle varies.

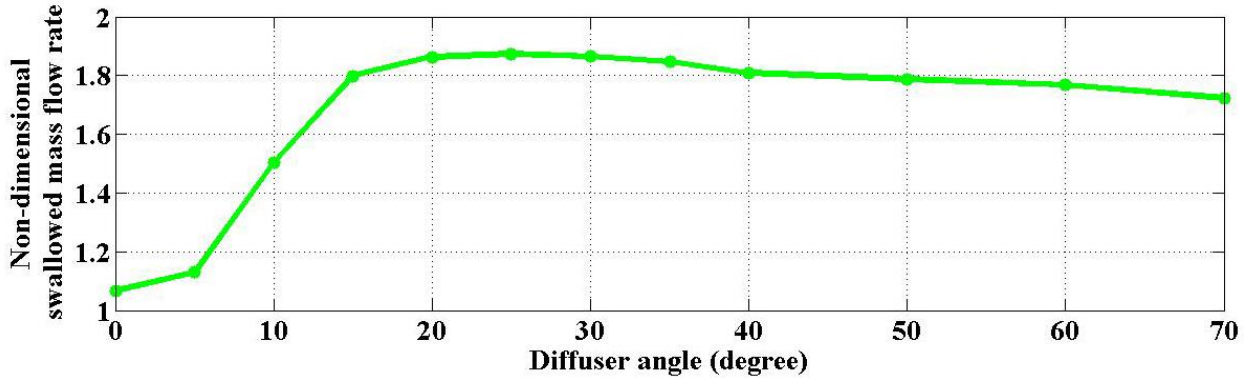

(a)

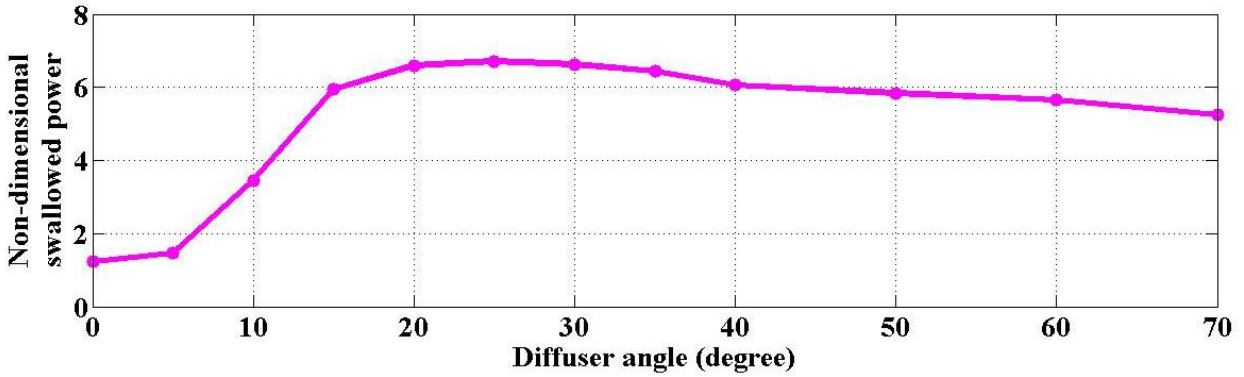

(b)

Fig. 15. Effect of diffuser angle ($\theta_{diffuser}$). (a) Non-dimensional swallowed mass flow rate vs $\theta_{diffuser}$ and (b) Non-dimensional swallowed power vs $\theta_{diffuser}$.

When the angle of the diffuser starts increasing from zero, the camber of the airfoil (longitudinal section of the duct shown in fig. 12) starts increasing as well that results in increase in the circulation and suction and finally increase in the swallowed flow by the duct. With further increase in the diffuser angle, separation occurs and creates a low pressure region at the outlet of the duct that causes the swallowed mass diagram continue increasing. But with further increase in the diffuser angle, the separated region spreads too much that results in a decrease in the swallowed flow.

4.2.6. Effect of diffuser radius ($R_{diffuser}$)

Effect of diffuser radius ($R_{diffuser}$) is studied in this part and the results are shown in fig. 16. All other geometric parameters are fixed as in tab.1 and only the diffuser radius varies.

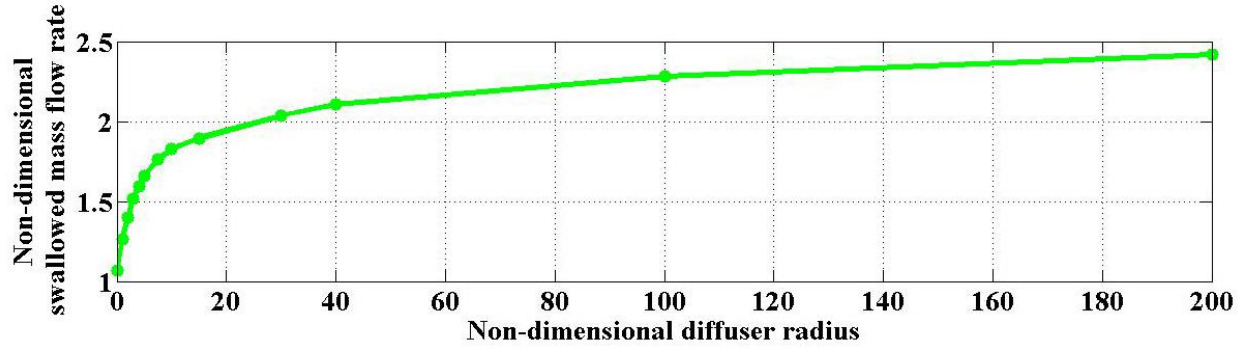

(a)

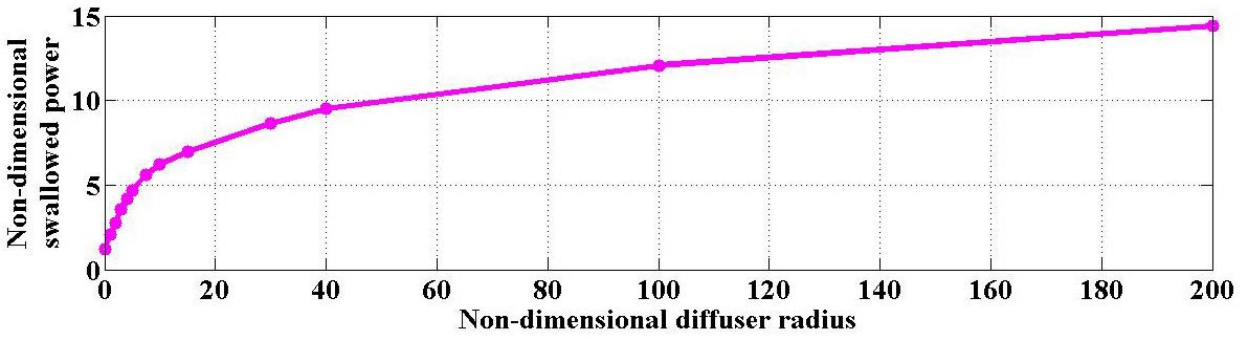

(b)

Fig. 16. Effect of non-dimensional diffuser radius ($R_{diffuser}/R_{throat}$). (a) Non-dimensional swallowed mass flow rate and (b) Non-dimensional swallowed power.

As the diffuser radius starts increasing from zero, the generated circulation of the airfoil (longitudinal section of the duct shown in fig.12) starts increasing that results in increase in the swallowed flow. With further increase in the diffuser radius, the separation occurs and the low pressure in the separated region at the outlet causes the swallowed flow diagram continue increasing. But, the larger the diffuser radius, the lower the body curvature of the diffuser. as the diffuser angle rises, the flow senses a smaller adverse pressure gradient that postpones the separation and results in increase in the swallowed flow. Although spreading of the separated region has a decreasing effect on the swallowed flow, but the increasing effect due to the separation postpone is dominant and the diagram continues its increasing trend. When the diffuser radius increases too much, the diffuser body becomes like a simple cone and the sensitivity of the adverse gradient to the body curvature decreases. Considering the diffuser longitudinal section as an arc of a circle, by simple geometrical analysis can show:

$$\lim_{R_{diffuser}\to\infty} \frac{\partial}{\partial R_{diffuser}}\left(\frac{\partial A_{diffuser\,(x)}}{\partial x}\right) = 0 \qquad (18)$$

Where x is the axial distance from the throat cross section in the direction of the free stream flow, $R_{diffuser}$ is the curvature radius of the diffuser body, and $A_{diffuser\,(x)}$ is the area of diffuser cross section at distance x from the throat. As can be seen in fig. 16, the sensitivity to the diffuser radius goes to zero as the diffuser radius rises to infinity.

4.2.7. Comparing the influence of the geometric parameters of a single-stage duct on the duct performance

In this section, the potential impact of the four discussed affecting geometric parameters of a single-stage duct on the duct performance is studied. The range of the changes in the independent geometric affecting parameters as well as the range of the corresponding changes in the swallowed power is expressed in tab.

4. Fig. 17 shows the potential impact of the four mentioned parameters using the specified indices 1 to 4. The value of the non-dimensional swallowed power related to the reference duct (tab. 1) is chosen as the reference to calculate the relative augmentation percent values in tab. 4 and fig. 17. As can be seen in fig. 17, the range of the

$parameter_{index}$	description	The range of the Changes	The range of the corresponding changes in relative swallowed power (%)
P_1	θ_{nozzle}	0° - 80°	[-48.4 , 6.3]
P_2	non-dimensional R_{nozzle} (R_{nozzle} /R_{throat})	0 - 10	[-55.6 , 10.8]
P_3	$\theta_{diffuser}$	0° - 70°	[-81.8 , 0.0]
P_4	non-dimensional $R_{diffuser}$ ($R_{diffuser}$ /R_{throat})	0 - 200	[-81.8 , 112.0]

Table 4. List of the geometric affecting parameters of a single-stage duct, the specified indices, and the ranges of the changes.

changes in duct performance due to changing the diffuser parameters is wider than the range of the changes caused by changing the nozzle parameters. Also, the range of the changes in duct performance caused by changing the angle is smaller than the range of change caused by changing the radius.

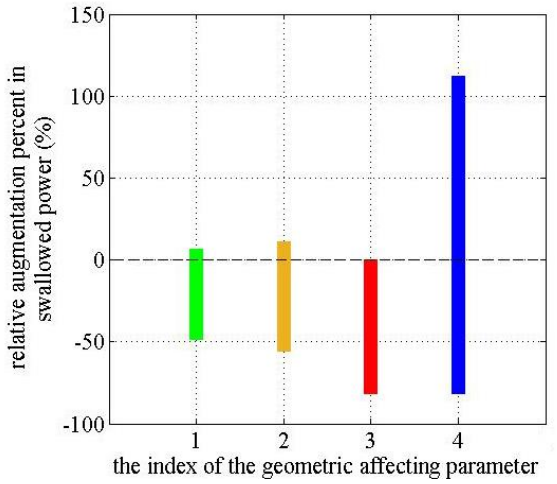

Fig. 17. A comparison between the potential impact of the four geometric affecting parameters of a single-stage duct. Indices 1 to 4 are specified to the affecting parameters in table 4.

4.3. Dual-stage inducing duct analysis

4.3.1. General description

In this part ducts with two stages are studied. Fig. 18 shows the contours of pressure, velocity, and streamlines of the flow field around a dual-stage duct. All details of the simulation are given in tables 2, 3, 5.

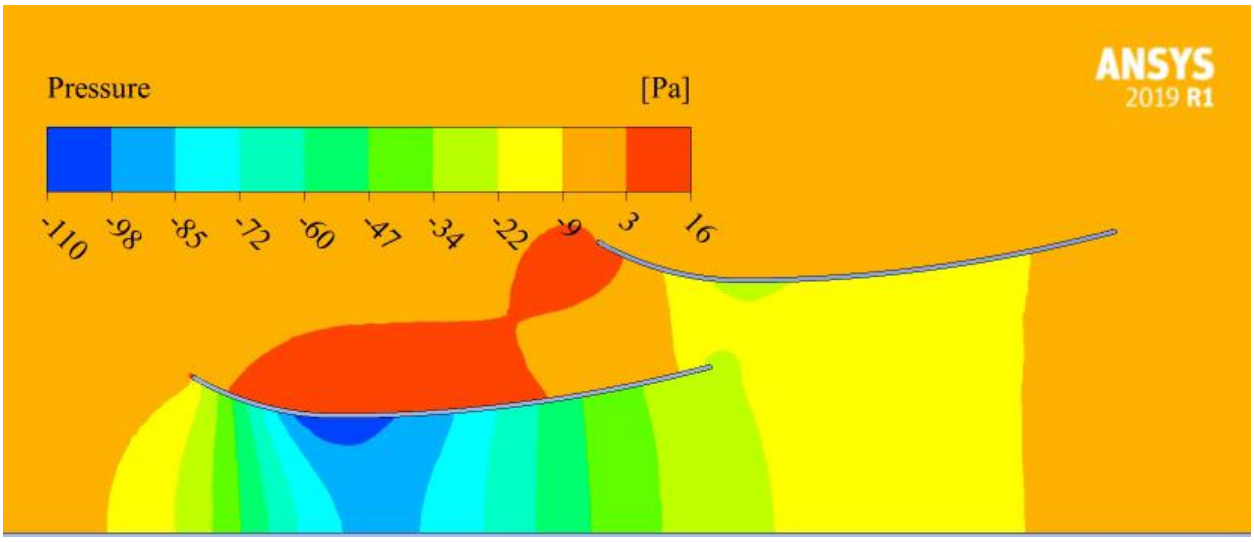
Pressure
[Pa]
-110
-98
-85
-72
-60
-47
-34
-22
-9
3
16
ANSYS
2019 R1

(a)

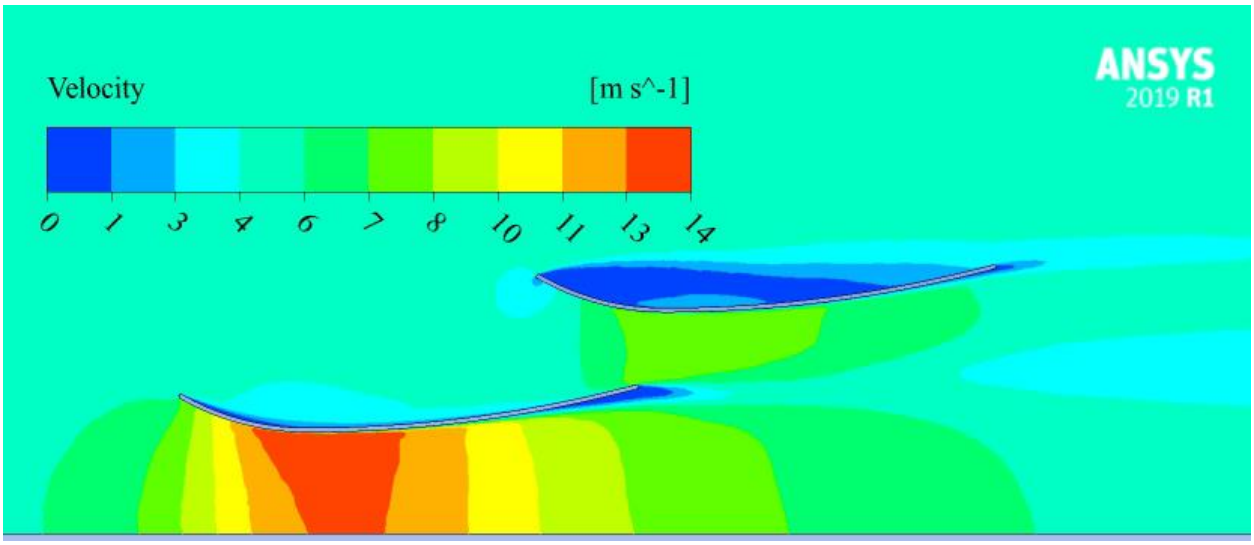
Velocity
[m s^-1]
0
1
3
4
6
7
8
10
11
13
14
ANSYS
2019 R1

(b)

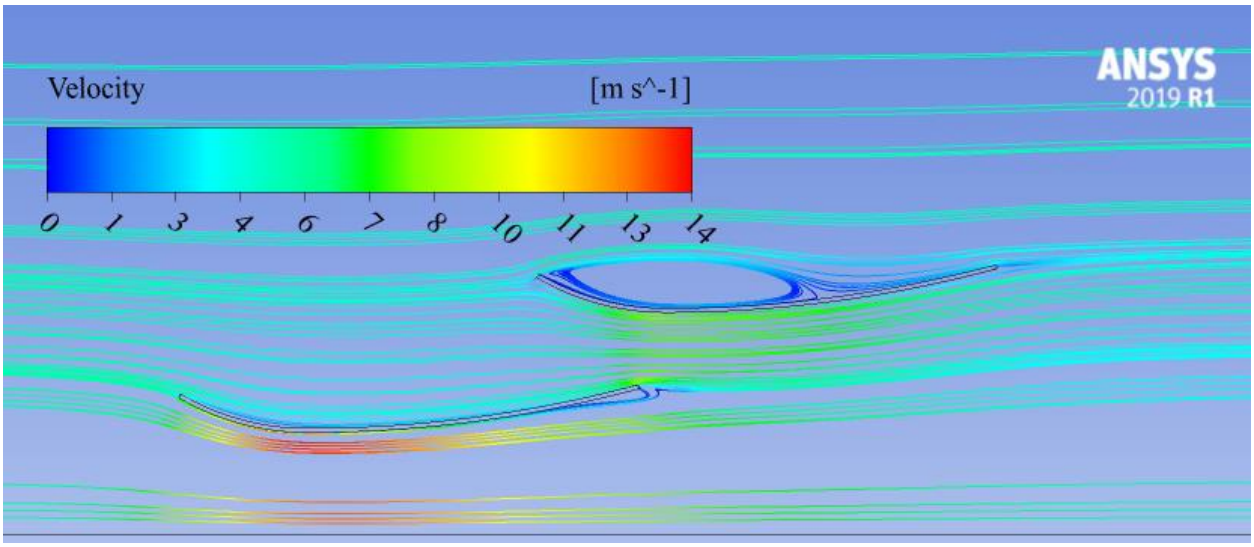

(c)

Fig.18. flow field around a dual-stage duct: contour of pressure distribution (a); contour of velocity distribution (b); streamlines(c).

4.3.2. Test plan (for dual-stage tests)

The schematic of a dual-stage inducing duct simulated in this section is shown in fig. 19. Studying effect of adding the second stage and the relative locations of the stages is the purpose in this part. Values specified to geometrical parameters of both stages are fixed, and the same as those specified in previous section (tab. 1). A dual-stage duct with a certain geometry is chosen as the reference case for all simulations of dual-stage ducts in this part (tab. 5).

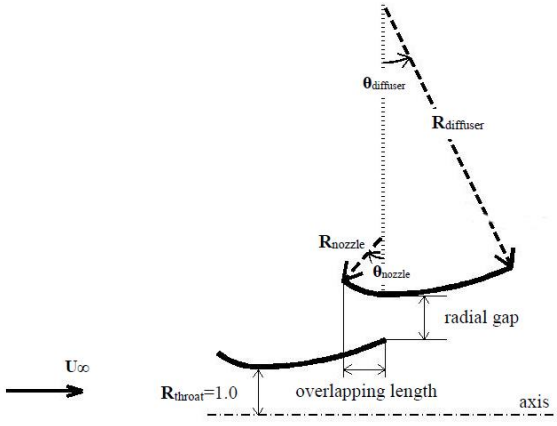

Fig. 19. Schematic of a dual-stage inducing duct. All lengths are non-dimensional (dividing by $R_{throat,stage1}$).

$R_{throat,stage1}$ (the reference length)	0.1 m
non-dimensional $R_{nozzle,stage1}$ ($R_{nozzle,stage1}$/ $R_{throat,stage1}$)	0.75
$\theta_{nozzle,stage1}$	30°
non-dimensional $R_{diffuser,stage1}$ ($R_{diffuser,stage1}$/ $R_{throat,stage1}$)	12.5

$\theta_{diffuser,stage1}$	24°
non-dimensional radial $gap_{stages1-2}$ (radial $gap_{stages1-2}$/ $R_{throat,stage1}$)	0.713
non-dimensional overlapping $length_{stages1-2}$ (overlapping $length_{stages1-2}$/ $R_{throat,stage1}$)	1.0
non-dimensional $R_{nozzle,stage2}$ ($R_{nozzle,stage2}$/ $R_{throat,stage1}$)	0.75
$\theta_{nozzle,stage2}$	30°
non-dimensional $R_{diffuser,stage2}$ ($R_{diffuser,stage2}$/ $R_{throat,stage1}$)	12.5
$\theta_{diffuser,stage2}$	24°

Table 5. geometrical parameters of the reference case chosen for all dual-stage tests. The value of 0.713 for non-dimensional radial $gap_{stages1-2}$ refers to the state at which the radial $gap_{stages1-2}$ is half the first stage diffuser outlet radius.

4.3.3. Effect of radial gap

The effect of the radial gap between two stages is studied in this part and the results are shown in fig. 20. All other geometric parameters are fixed as in the reference case and only the radial gap varies.

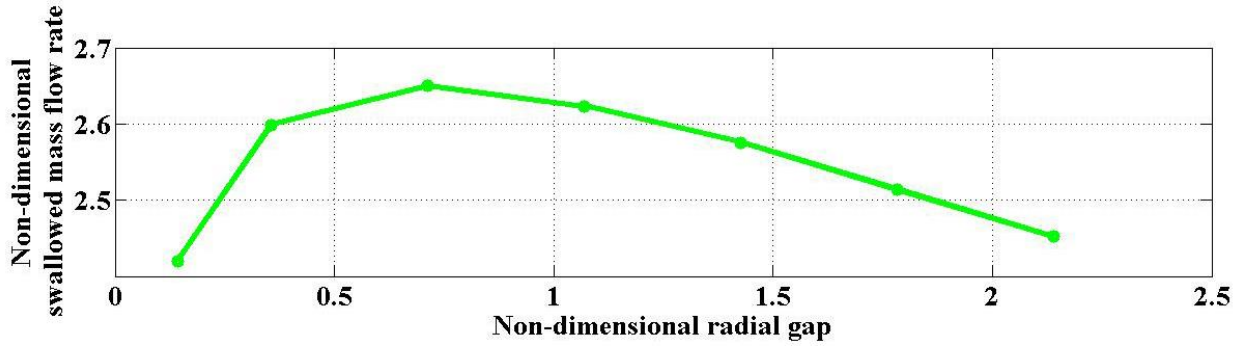

(a)

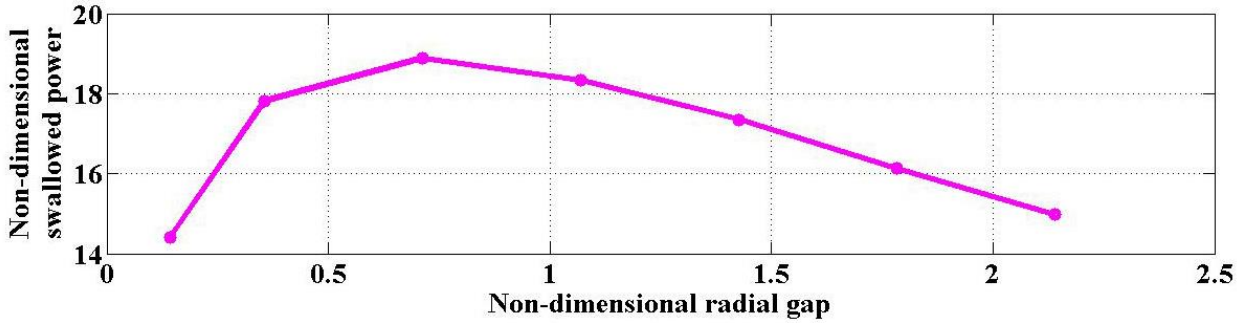

(b)

Fig. 20. Effect of non-dimensional radial $gap_{stages1-2}$ (radial $gap_{stages1-2}$/$R_{throat,stage1}$). (a) Non-dimensional swallowed mass flow rate; and (b) Non-dimensional swallowed power.

As shown in fig. 19, stages overlapping creates a converging channel between the stages that causes the flow to accelerate passing the radial gap between the stages. When the radial gap is too small, the blockage effect causes a decrease in the suction. As the radial gap grows, the blockage effect is weakened and the suction increases. But too much increase in the radial gap causes the converging coefficient of the channel between the stages to decrease too much and results in a decrease in the created suction.

4.3.4. Effect of the overlapping length

The effect of overlapping length between two stages is studied in this part and the results are shown in fig. 21.

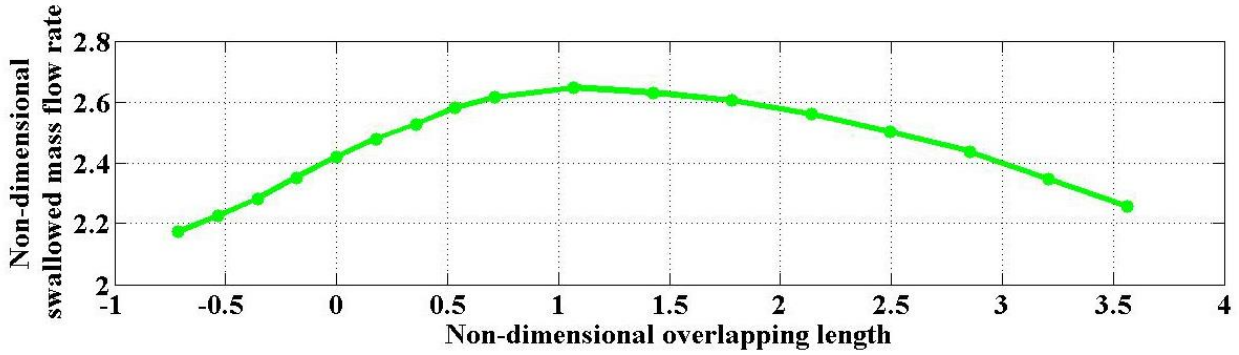

(a)

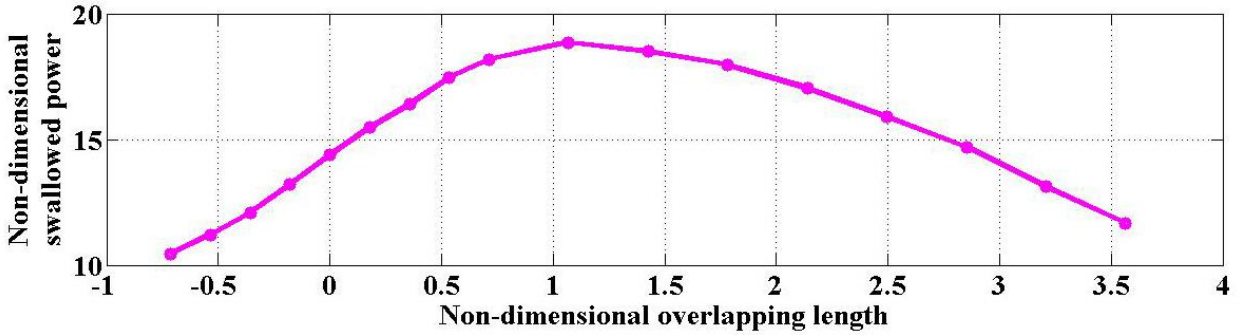

(b)

Fig. 21. Effect of non-dimensional overlapping length$_{stages1\text{-}2}$ (overlapping length$_{stages1\text{-}2}$ /$R_{throat,stage1}$). (a) Non-dimensional swallowed mass flow rate; and (b) Non-dimensional swallowed power

When the overlapping length increases from negative amounts to positive amounts, as shown in fig. 19, stages overlapping creates a converging channel between the stages. Due to the specific shape of the stages, an increase in overlapping length results in an increase in the geometrical converging coefficient of the created gap channel between the stages. At first that the positive overlapping length is small and the geometrical converging ratio of the gap channel is not too large to cause a blockage in the flow field, increase in overlapping length causes an increase in the suction. But with a further increase in the overlapping length, the blockage effect occurs that results in a decrease in the suction.

4.3.5. Comparison of the influence of the geometric parameters related to the consecutive stages in a dual-stage duct on the duct performance

Fig. 22 shows the potential impact of the parameters mentioned in tab. 6. The value of the swallowed power related to the reference dual-stage duct (tab. 5) is chosen as the reference to calculate the relative augmentation percent values in fig. 22. Since the radial gap and overlapping length are geometric parameters that depend on the geometry of both stages, there is no set rule to determine which of the two parameters is more effective. Depending on the geometry of the two consecutive stages, one or another parameter may be more effective.

$parameter_{index}$	description	The range of the Changes	The range of the corresponding changes in the swallowed power (%)
P_1	non-dimensional radial $gap_{stages1-2}$ ($gap_{stages1-2}$/ $R_{throat,stage1}$)	[0.1426 , ∞)	[-64.1 , 0.0]
P_2	non-dimensional overlapping $length_{stages1-2}$ ($length_{stages1-2}$/ $R_{throat,stage1}$)	[-0.713 , ∞)	[-64.0 , 0.0]

Table 6. List of the geometric affecting parameters related to the consecutive stages in a dual-stage duct, the specified indices, and the ranges of the changes.

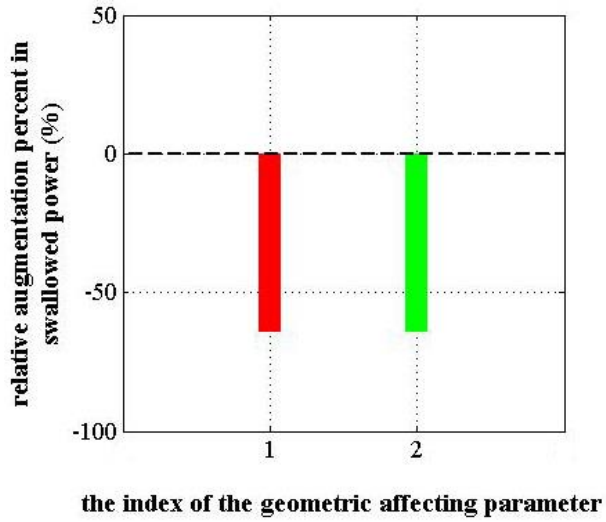

Fig. 22. A comparison between the potential impact range of the geometric affecting parameters related to the consecutive stages in a dual-stage duct. Indices 1 and 2 are specified to the affecting parameters in the tab. 6.

4.4 Multi-stage analysis

4.4.1. General description

In this part, ducts with several stages are investigated. Fig. 23 shows the contours of pressure, velocity and streamlines of the flow field around a three-stage duct. As can be seen in fig. 23, inducing effect due to adding the third stage causes a significant increase in the first stage velocity compared to fig. 18.

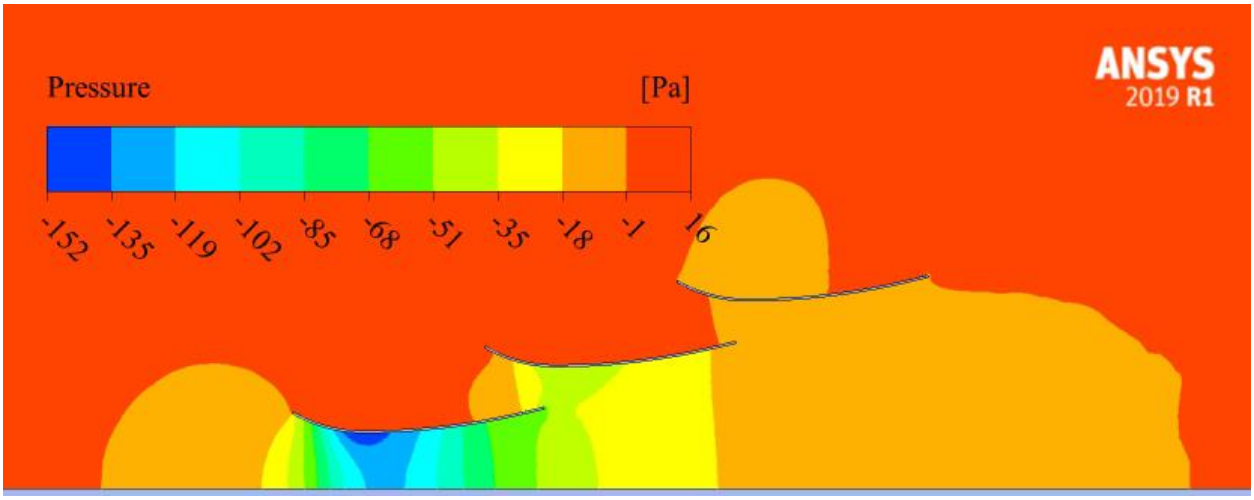
Pressure
[Pa]
-152
-135
-119
-102
-85
-68
-51
-35
-18
-1
16
ANSYS
2019 R1

(a)

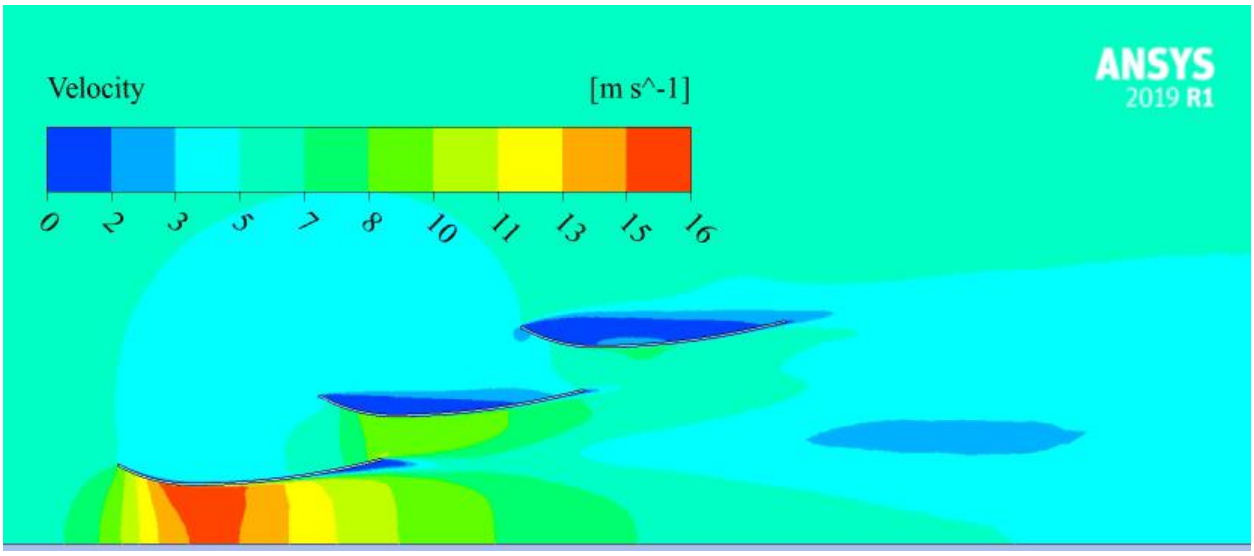
Velocity
[m s^-1]
0
2
3
5
7
8
10
11
13
15
16
ANSYS
2019 R1

(b)

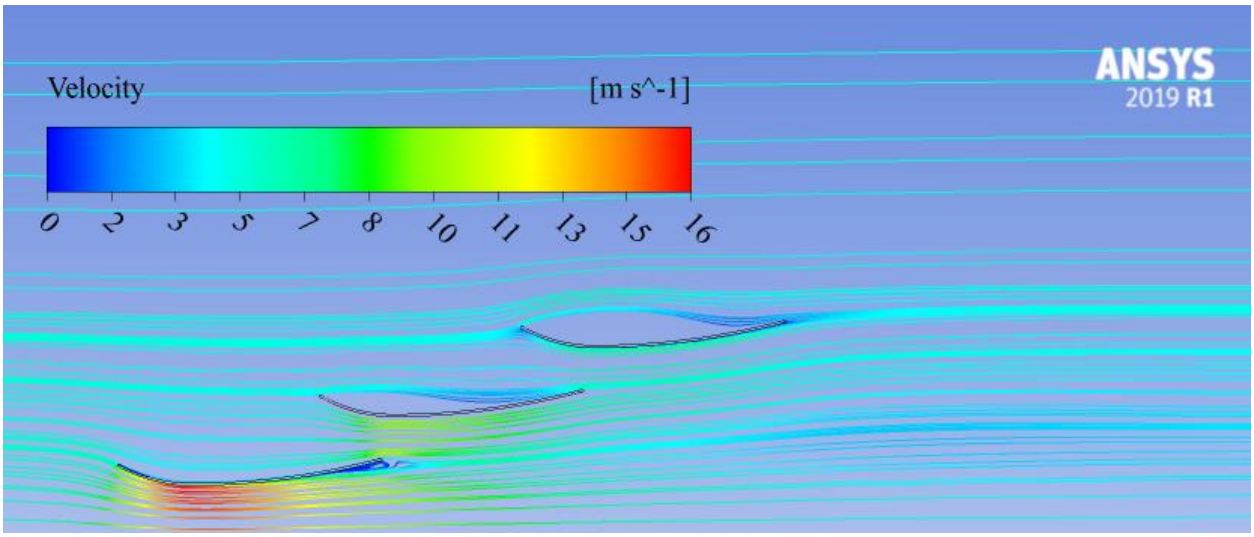

(c)

Fig.23. flow field around a multi-stage (three-stage) duct: contour of pressure distribution (a); contour of velocity distribution (b); streamlines(c).

4.4.2. Test plan (for multi-stage tests)

In this section, various multi-stage ducts with the number of stages from 1 to 24 are simulated. Since we intend to study the effect of the number of the stages, longitudinal sections of all stages are chosen the same for simplicity. Also, the radial gaps and the overlapping lengths between all of the stages are chosen the same as well (tab. 5).

4.4.3. Effect of the number of the stages

In this part, Multi-stage ducts up to 24 stages are simulated and the results are shown in fig. 24. As can be seen in fig. 24, as the number of the stages increases, the slope of the diagram decreases. It shows that the first stages are more effective than the last ones. In fact, the later downstream stages need their previous stages as intermediates to be able to affect the mass flow rate swallowed by the first stage. Obviously the more the number of the intermediate stages, the less the inducing effect on the first stage.

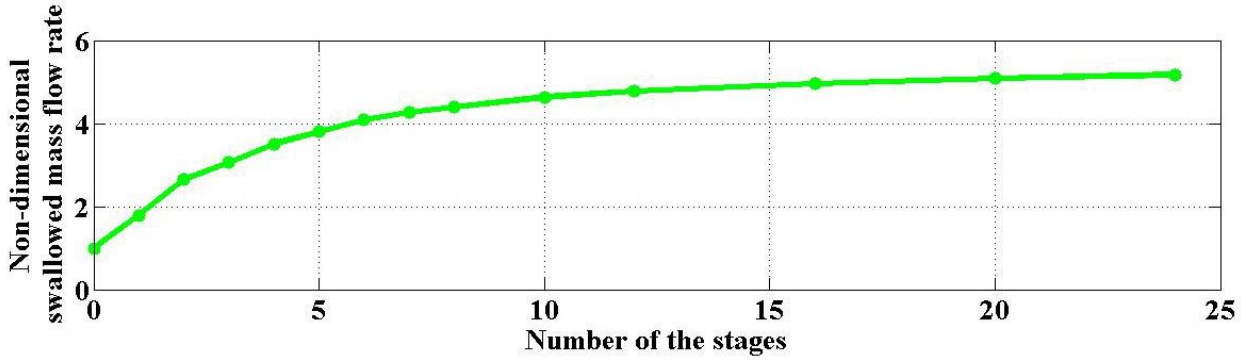

(a)

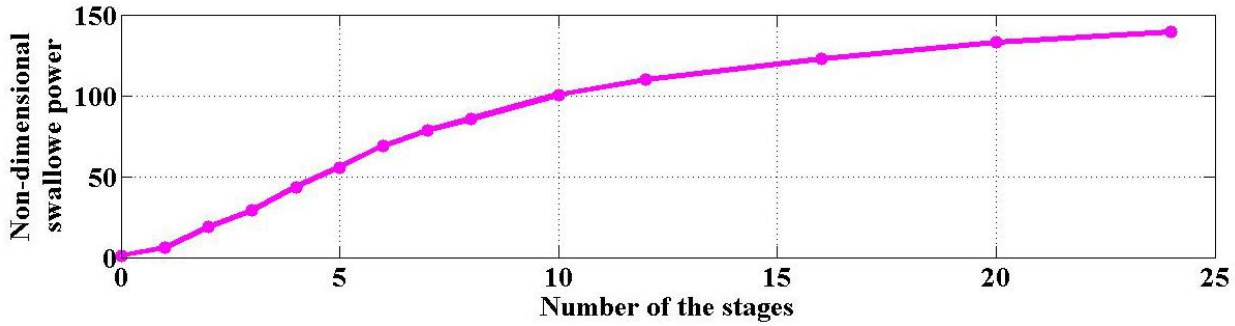

(b)

Fig. 24. Effect of the number of stages. (a) Non-dimensional swallowed mass flow rate vs the number of the stages; and (b) Non-dimensional swallowed power vs the number of the stages.

4.4.4. Effect of the wind velocity on the performance of the multi-stage inducing ducts

Fig. 25 shows the average axial velocity at the first stage throat of the ducts with the various number of the stages at various wind velocities. Except for velocity that varies in this section, all other properties of the free stream are the same as given in the tab. 3. As can be seen in the figure, when the number of the stages is very low the diagrams are obviously steep and when the number of the stages increases to high numbers, the slope of the diagrams approaches zero. That means, as mentioned in the previous section, the first stages are more effective than the last ones. But, as fig. 25 shows, diagrams of different wind velocities have different behaviors. The diagrams' slope is larger at higher wind velocities compared to lower wind velocities. It can be seen more obviously in ducts with one or two stages, and as the number of the stages increases, the slope of the diagrams of higher wind velocities approach zero slower than those of the lower velocities. Because at the higher wind speeds, compared to the lower wind speeds, the inducing suction effect is stronger and therefore causes a stronger increase in the swallowed mass flow rate at the first stage throat. In other words, the performance of a multi-stage inducing duct improves at higher free stream velocities.

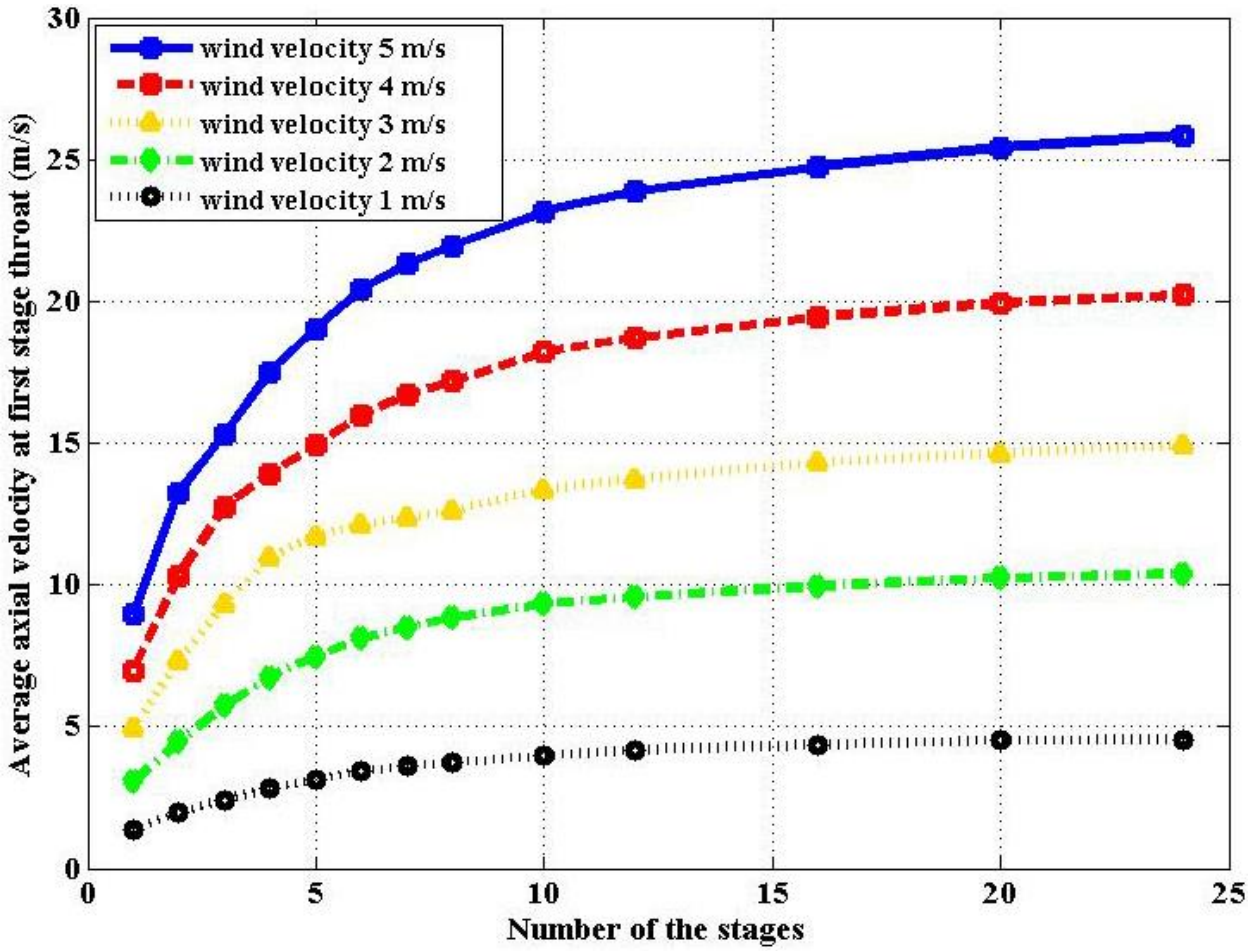

Fig. 25. Effect of the number of stages on the performance of a multi-stage inducing duct at various wind velocities.

The absolute augmentation percent in swallowed power (AAP_{SP}) is defined as follows:

$$AAP_{S_P} = \frac{swallowed\ power - reference\ power}{reference\ power} * 100\% \qquad (19)$$

Where the swallowed power and the reference power are computed from eq. (15) and eq. (16), respectively.

4.4.5. deciding on the number of the stages of a multi-stage inducing duct

In contrast to the absolute augmentation percent in swallowed power, the relative augmentation percent in swallowed power (RAP_{SP}) is defined as follows:

$$RAP_{S_P} = \frac{SP_N - SP_{N-1}}{SP_{N-1}} * 100\% \qquad (20)$$

Where SP_N is the swallowed power after the N^{th} stage is added, SP_{N-1} is the swallowed power before the N^{th} stage is added, and values of swallowed power (SP_N and SP_{N-1}) are computed from eq. (15). Fig. 26 shows the diagram of the relative augmentation percent in swallowed power as the number of the stages increases from N-1 to N. As can be seen in fig. 27, as the N grows, the relative effectiveness of adding the N^{th} stage to the existing duct with N-1 stages decreases continuously whereas, the absolute effectiveness of the new-added stage (N^{th} stage), as fig. 25 shows, increases continuously. On the other hand, the last stages are

larger, heavier, and further away from the turbine, and therefore, the costs of manufacturing the stages and building the necessary equipment for structural support significantly increase at the last stages. Although, according to the absolute diagrams like fig. 24b and fig. 25, the more the number of the stages, the more the swallowed power but, the relative diagram illustrated in fig. 27 along with some economic considerations on the costs of manufacturing the stages and building the needed equipment for structural support, help us to decide on the number of the stages. In most applications, choosing two, three, or four stages is enough to achieve an acceptable result, and it is not economical to use more.

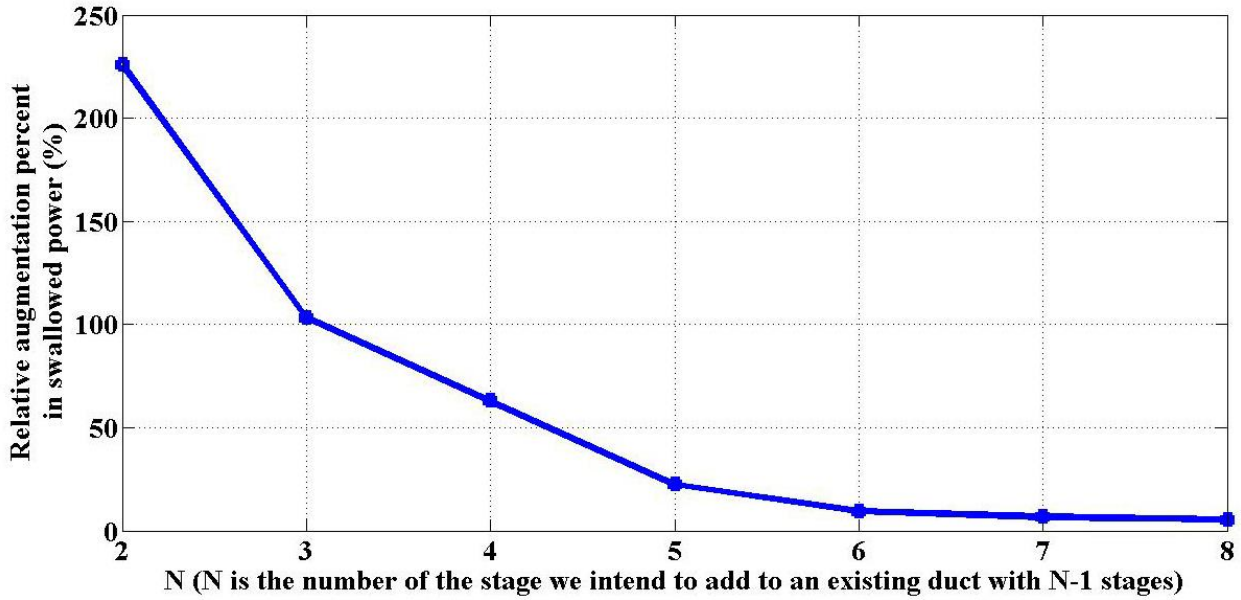

Fig. 26. Diagram of the relative effectiveness of adding the N^{th} stage to an existing duct with (N-1) stages, defined by eq. (20).

5. Conclusion

In this study a specific configuration of the duct, called Multi-Stage Inducing Duct, was presented, numerically simulated, and effects of its geometrical parameters were investigated. It was shown that using a multi-stage inducing duct causes a significant increase in the wind velocity profile. In a multi-stage inducing duct, the downstream stages induce a suction effect on the upstream stages. When there is only one stage, there is no inducing effect and only some suction is produced due to the nozzle-diffuser shape of the stage. The effect of the geometrical parameters of a single-stage duct was investigated and it was concluded that the parameters of the diffuser part are more effective than the parameters of the nozzle part. Also, it was observed that the range of the changes in the swallowed power caused by the changes in the radius is wider than the range of the changes caused by the changes in the angle, in both nozzle and diffuser parts. When the second stage is added, the inducing effect occurs and the suction produced by the second stage helps the flow to exit easier from the first stage outlet, and consequently, the more mass flow rate is swallowed by the first stage. The effects of changes in the radial gap and overlapping length between two consecutive stages on inducing effect were studied separately and it was shown that increase in the radial gap between two consecutive stages, at first increases and then decreases the induced suction at the first stage throat. Similar behavior was observed when the overlapping length between two consecutive stages increased. Comparing the impact of the radial gap and overlapping length showed that they are of the same power of influence, and none is negligible compared to the other. Effects of the number of the stages and

the free stream velocity on the duct performance were studied together and it was shown that the last stages are less effective than the first ones due to their higher distance from the first stage throat. It was shown that the strength of the inducing effect depends on the free stream velocity and the higher the free stream velocity, the higher the effectiveness of the downstream stages. Finally, the effectiveness of adding a new stage to an existing multi-stage inducing duct was studied from two different points of view: absolute effectiveness and relative effectiveness. It was shown that although the higher the number of the stages, the greater the swallowed power from an absolute point of view, but, from a relative point of view, it is not usually economic to use more than three or four stages due to high costs of manufacturing and building the equipment needed for structural support.

Abbreviations

NDSMFR	non-dimensional swallowed mass flow rate
AAP_{SP}	absolute augmentation percent in swallowed power
RAP_{SP}	relative augmentation percent in swallowed power
SP_N	swallowed power by a N-stage duct (after the N^{th} stage be added)
SP_{N-1}	swallowed power by a (N-1)-stage duct (before the N^{th} stage be added)

Nomenclature

ρ	Fluid density
P	Static pressure
g_i	component of the gravitational acceleration in the i^{th} spatial direction
t	time
δ_{ij}	Kronecker delta
F_i	component of the body force in the i^{th} spatial direction
τ_{ij}	Reynolds stress tensor
u_i	component of the velocity in the i^{th} spatial direction
x_i	component of the length in the i^{th} spatial direction
μ	Fluid viscosity
u_i'	turbulent velocity fluctuation in the i^{th} spatial direction
k	Turbulence kinetic energy
ω	turbulence specific dissipation rate
U_∞	free stream velocity
r	radial distance from the duct axis at the first stage throat plane
$V_{axial\ (r)}$	axial velocity as a function of r
x	axial distance from the throat cross section in the direction of the free stream flow
R_{throat}	radius of the first stage throat cross section
A_t	area of the first stage throat cross section
θ_{nozzle}	arc angle of the nozzle body
$\theta_{diffuser}$	arc angle of the diffuser body

R_{nozzle}	curvature radius of the nozzle body
$R_{diffuser}$	curvature radius of the diffuser body
$A_{diffuser\ (x)}$	area of diffuser cross section at the distance x from the throat

References

1. Tahani, M., Babayan, N., Mehrnia, S.M., and Shadmehri, M. "A novel heuristic method for optimization of straight blade vertical axis wind turbine", Energy Conversion and Management, **127**, pp. 461–476 (2016).
2. Tahani, M., Rabbani, A., Kasaeian, A., Mehrpooya, M., and Mirhosseini, M. "Design and numerical investigation of Savonius wind turbine with discharge flow directing capability", Energy, **130**, pp. 327-338 (2017).
3. Tahani, M., Maeda, T., Babayan, N., Mehrnia, S.M., Shadmehri, M., Li, Q., Fahimi. R., and Masdari, M. "Investigating the effect of geometrical parameters of an optimized wind turbine blade in turbulent flow", Energy Conversion and Management, **153**, pp. 71-82 (2017).
4. Tahani, M., Kavari, G., Masdari, M., and Mirhosseini, M. "Aerodynamic design of horizontal axis wind turbine with innovative local linearization of chord and twist distributions", Energy, **131**, pp. 78-91 (2017).
5. Tahani, M., Babayan, N., and Pouyaei, A. "Optimization of PV/Wind/Battery stand-alone system, using hybrid FPA/SA algorithm and CFD simulation, case study: Tehran", Energy Conversion and Management, **106**, pp. 644-659 (2015).
6. Abe, K., Nishida, M., Sakurai, A., Ohya,Y., Kihara, H., Wada, E., and Sato, K. "Experimental and numerical investigations of flow fields behind a small wind turbine with a flanged diffuser", Wind Engineering, **93**(12), pp. 951-970 (2005).
7. Ohya, Y., Karasudani, T., Sakurai, A., Abe, K., and Inoue, M. "Development of a shrouded wind turbine with a flanged diffuser", J. of Wind Engineering and Industrial Aerodynamics, **96**, pp. 524-539 (2008).
8. Kosasih, B., and Tondelli, A. "Experimental study of shrouded micro-wind turbine", Procedia Engineering, **49**, pp. 92-98 (2012).
9. Jafari, S., and Kosasih, B. "Flow analysis of shrouded small wind turbine with a simple frustum diffuser with computational fluid dynamics simulations", Wind Engineering and Industrial Aerodynamics, **125**, pp. 102-110 (2014).
10. Mansour, K., and Meskinkhoda, P. "Computational analysis of flow fields around flanged diffusers", Wind Engineering and Industrial Aerodynamics, **124**, pp. 109-120 (2014).
11. Zabihzade, S., Alimirzazadeh, S., and Rad, M. "RANS simulations of the stepped duct effect on the performance of ducted wind turbine", Wind Engineering and Industrial Aerodynamics, **145**, pp. 270-279 (2015).
12. Han, W., Yan, P., Han, W., and He, Y. "Design of wind turbines with shroud and lobed ejectors for efficient utilization of low-grade wind energy", Energy, **89**, pp. 687-701 (2015).
13. Al-Sulaiman, F. "Exergoeconomic analysis of ejector-augmented shrouded wind turbines", Energy, **128**, pp. 264-270 (2017).

14. Khamlaj, T.A., Rumpfkeil, M.P. “Analysis and optimization of ducted wind turbines”, Energy, **162**, pp. 1234-1252 (2018).
15. Saleem, A., Kim, M. “Effect of rotor tip clearance on the aerodynamic performance of an aerofoil-based ducted wind turbine”, Energy Conversion and Management, **201**, pp. 1-14 (2019).
16. Noorollahi, Y., Ghanbari, S., and Tahani, M. “Numerical analysis of a small ducted wind turbine for performance improvement”, Int. J. of Sustainable Energy, **39**(3), pp. 290-307 (2020).
17. Keramat, N., Najafi, G., Tavakkoli, T., Ghobadian, B., and Mahmoodi, E. “An innovative variable shroud for micro wind turbines”, Renewable Energy, **145**, pp. 1061-1072 (2020).
18. Bontempo, R., and Manna, M. “Diffuser augmented wind turbines: Review and assessment of theoretical models”, Applied Energy, **280**, pp. 1-17 (2020).
19. Keramat, N., Najafi, G., Tavakkoli, T., Ghobadian, B., and Mahmoodi, E. “Mathematical modeling of a horizontal axis shrouded wind turbine”, Renewable Energy, **146**, pp. 856-866 (2020).
20. Prasad, K.R., Kumar, V.M., Swaminathan, G., and Loganathan, G.B. “Computational investigation and design optimization of a duct augmented wind turbine (DAWT)”, Mater. Todays: proceedings, **22**(3), pp. 1186-1191 (2020).
21. Rivarolo, M., Freda, A., and Traverso, A. “Test campaign and application of a small-scale ducted wind turbine with analysis of yaw angle influence”, Applied Energy, **279**, pp. 1-9 (2020).
22. Avallone, F., Ragni, D., and Casalino, D. “On the effect of the tip-clearance ratio on the aeroacoustics of a diffuser-augmented wind turbine”, Renewable Energy, **152**, pp. 1317-1327 (2020).
23. Nardecchia, F., Groppi, D., Garcia, D.A., Bisegna, F., and Santoli, L. “A new concept for a mini ducted wind turbine system”, Renewable Energy, **175**, pp. 610-624 (2021).
24. Menter, F.R., Kuntz, M., and Langtry, R. “Ten Years of Industrial Experience with the SST Turbulence Model”, Turbulence, Heat and Mass Transfer, **4**, pp. 625-632 (2003).

Biographies

Mojtaba Tahani is an associate professor in Faculty of New Sciences and Technologies (FNST), University of Tehran, Amiraabad shomali, Tehran, Iran. He obtained his PhD in Iran University of Science and Technology. His fields of research are CFD, Turbulence flows, Aerodynamics, Fluid mechanics and Thermodynamics.

Mehran Masdari is an assistant professor at University of Tehran. He is holding Bsc. Eng., MSc. and Ph.D. degrees in Aerodynamics from Sharif University of Technology. He published more than 50 scientific papers in English and Persian. He has 15 years of job experience both in industry and academic fields. Various aerospace courses and student projects were conducted by him. His research interests: Transitional flows, Applied aerodynamics, Experimental Fluid Dynamics, Particle image velocimetry (PIV), Bluff body wakes, Turbulent boundary layer, Wind Engineering, Mechanical Engineering, Fluid Mechanics, Aerodynamics, Turbomachinery, Turbulence, Wind turbine, Vertical Axis Wind Turbine (VAWT), Micro Air Vehicles, Fluid Mechanics, Aerospace Engineering, Fluid Dynamics, Wind Tunnel Testing, Neural Network and Data Processing.
E-mail: m.masdari@ut.ac.ir

Amin Habibi is a Ph.D. candidate in aerospace engineering (aerodynamics) in Faculty of New Sciences and Technologies, university of Tehran, Tehran, Iran. His main research direction is wind engineering and computational fluid dynamics (CFD).

Mojtaba Mirhosseini graduated with a PhD in energy engineering from Aalborg University, Denmark. Now, he is an assistant professor in School of Advanced Technologies at Iran University of Science and Technology (IUST), Tehran, Iran. His research focuses on energy systems engineering and renewable energy technologies. One of his research interests and specialties is aerodynamics of wind turbines.